Research in Astronomy and Astrophysics, 24:015020 (20pp), 2024 January https://doi.org/10.1088/1674-4527/ad0689

A Rendezvous Mission to the Second Earth Trojan Asteroid 2020 XL_5 with Low-Thrust Multi-Gravity Assist Techniques

Shi-Hai Yang, Bo Xu, and Xin Li
School of Aeronautics and Astronautics, Sun Yat-sen University, Shenzhen 518107, China; xubo27@mail.sysu.edu.cn
Received 2023 March 10; revised 2023 October 10; accepted 2023 October 13; published 2024 January 9

Abstract

As the second of Earth's Trojan asteroids, 2020 XL_5 is worthy of rendezvous and even sample return missions in many aspects. In this paper, a rendezvous mission to Earth's second Trojan asteroid 2020 XL_5 is proposed. However, due to its high inclination and large eccentricity, direct impulsive transfer requires large amounts of fuel consumption. To address this challenge, we explore the benefits of electric propulsion and multi-gravity assist techniques for interplanetary missions. These two techniques are integrated in this mission design. The design of a low-thrust gravity-assist (LTGA) trajectory in multi-body dynamics is thoroughly investigated, which is a complex process. A comprehensive framework including three steps is presented here for optimization of LTGA trajectories in multi-body dynamics. The rendezvous mission to 2020 XL_5 is designed with this three-step approach. The most effective transfer sequence among the outcomes involves Earth–Venus–Earth–Venus-2020 XL_5. Numerical results indicate that the combination of electric propulsion and multi-gravity assists can greatly reduce the fuel consumption, with fuel consumption of 9.03%, making it a highly favorable choice for this rendezvous mission.

Key words: minor planets – asteroids: general – celestial mechanics – Planetary Systems

1. Introduction

It was proved in 1772 that there are two groups of small bodies which can stably share the orbit of a planet if they remain near the triangular point 60° ahead (L_4 point) or behind (L_5 point) it in its orbit (Connors et al. 2011). The first discovery of these Trojan asteroids dates back to 1906, when Max Wolf found 588 Achilles (Nicholson 1961), orbiting around the triangular point 60° ahead of Jupiter along its orbit. Since then, more than 10,000 Trojans have been identified for Venus (De la Fuente Marcos & de la Fuente Marcos 2014), Mars (de La Fuente Marcos & de La Fuente Marcos 2013), Jupiter (Dvorak & Schwarz 2005), Uranus (de la Fuente Marcos & de la Fuente Marcos 2015) and Neptune (Sheppard & Trujillo 2006), with the majority being Jupiter Trojans. However, no Earth Trojan (ET) was identified until 2011. Asteroid 2010 TK_7 was observed in the Wide-field Infrared Survey Explorer (WISE) mission, and was found to be the first ET asteroid (Connors et al. 2011). As the current limits allow a population of perhaps 10^3 ETs with diameters greater than 100 m ($H \approx 23$) (Wiegert et al. 2000), there are more ETs to be discovered besides 2010 TK_7. However, due to the unfavorable viewing geometry of an object orbiting Earth–Sun's L_4 or L_5 points as seen from Earth (Malhotra 2019), all the dedicated surveys aimed at detecting new ETs found nothing (Wiegert et al. 1997; Whiteley & Tholen 1998; Markwardt et al. 2020; Lifset et al. 2021).

Asteroid 2020 XL_5 was discovered by the Panoramic Survey Telescope and Rapid Response System (Pan-STARRS) survey on 2020 December 12,[1] and was considered as a potential candidate of an ET asteroid (de la Fuente Marcos & de la Fuente Marcos 2021). Subsequent investigations, conducted through follow-up studies, solidified 2020 XL_5's identity as the second ET asteroid (Hui et al. 2021; Santana-Ros et al. 2022). Both 2010 TK_7 and 2020 XL_5 are classified as transient ETs, with their orbital stability around L_4 shown to be on the scale of thousands of years, far from the stability timescale of a theoretical primordial ET population (Santana-Ros et al. 2022). The inferred diameter for 2020 XL_5 is $1.18^{+0.08}_{-0.08}$ km with an assumed albedo of 0.06 ± 0.03 (Santana-Ros et al. 2022). This diameter is larger than that of the first ET asteroid 2010 TK_7, which was estimated to have a diameter of ∼0.3 km (Connors et al. 2011). Because of some non-gravitational effects like the Yarkovsky effect, the orbital motion is related to its physical and geological properties. The determination of such properties becomes crucial to study the origin and orbital evolution of the asteroid. Moreover, because ETs share the orbit of Earth, their chemical composition can greatly reflect the space environment of Earth. Therefore, ETs are significant candidates for rendezvous and even sample return missions.

However, due to the relatively high inclination and considerable eccentricity of both 2020 XL_5 and 2010 TK_7,

[1] https://www.minorplanetcenter.net/mpec/K20/K20XH1.html

reaching the targets directly from low Earth orbit (LEO) using chemical propulsion (CP) proves to be a costly mission. The minimum total delta-v for the rendezvous mission with ballistic trajectory varies between 7.9 and 10.3 km s^{-1} for 2020 XL_5, depending on the launch conditions. Meanwhile, for 2010 TK_7, this range is between 6 and 8.5 km s^{-1} (Santana-Ros et al. 2022). Thus, a rendezvous mission to 2020 XL_5 is much costlier than a mission to 2010 TK_7. Considering the delta-v budget, it is imperative to further optimize the trajectory for the rendezvous mission. For a mission to 2010 TK_7, there have been relevant studies about the optimization of transfer trajectory (Lei et al. 2017; Gao et al. 2019). The gravity-assist technique can be adopted to reduce the launch energy and rendezvous delta-v since it can effectively change the inclination of a spacecraft's trajectory. In two-body dynamics, numerical results show that the fuel consumption of an impulsive trajectory with a Venus-Earth-Venus swingby sequence is 41% with flight time of 1694 days (Lei et al. 2017). Moreover, electric propulsion (EP) is also an efficient technique to save the fuel consumption (Chen et al. 2018). EP was applied in the last leg of an impulsive transfer trajectory, i.e., from Venus to 2010 TK_7, transforming the impulsive leg into a low-thrust leg (Lei et al. 2017). The application of EP in the last leg reduced the fuel consumption to 4.59% with flight time of 1684 days, where the initial mass was 800 kg and the maximal magnitude of thrust was 120 mN. This work aims for the design of a rendezvous mission to the new ET asteroid 2020 XL_5. In this work, since the orbit of 2020 XL_5 has a high inclination together with a large eccentricity, EP and multi-gravity assist techniques are combined for the optimization of transfer trajectory.

There have been numerous studies about the optimization of a low-thrust transfer trajectory (Morante et al. 2021). Approaches to solve the fuel-optimal problem can be generally categorized into direct methods, indirect methods and hybrid methods. In the direct method, the fuel-optimal problem is converted into a parameter optimization problem and then nonlinear programming (NLP) can be applied to obtain the solution (Hargraves & Paris 1987). Direct methods do not require an accurate initial guess because of a large domain of convergence. Besides, the optimization variables have physically intuitive meanings. However, direct methods require a large amount of computation and may not converge to the optimal solution. As for an indirect method, the optimization problem is usually turned into a two-point boundary-value problem (TPBVP) or multi-point boundary-value problem (MPBVP) (Haberkorn et al. 2004; Jiang et al. 2012; Chen et al. 2018). Indirect methods provide assurances that the first-order necessary conditions are satisfied (Morante et al. 2021). Nevertheless, indirect methods normally require an appropriate initial guess and are usually difficult to solve due to the small convergence radius. Hybrid methods are combinations, which have the advantages of both methods, where the time histories of costate variables are directly parameterized and the optimal solution is obtained through the NLP method (Gao & Kluever 2004).

A multitude of research efforts has been dedicated to optimizing low-thrust gravity-assist (LTGA) trajectories (Casalino et al. 1999; McConaghy et al. 2003; Petropoulos & Longuski 2004; Vasile & Campagnola 2011; Jiang et al. 2012; Yang et al. 2015). A broad search algorithm with a simplified shape-based trajectory model was applied to generate initial estimates for Gravity-Assist, Low-Thrust, Local Optimization Program (GALLOP) (Petropoulos et al. 2000; Petropoulos & Longuski 2004). This algorithm was implemented in the software Satellite Tour Design Program for Low-Thrust Gravity-Assist (STOUR-LTGA), which automatically searches for low-thrust, gravity-assist trajectories. Subsequently, STOUR was utilized to conduct a broad search, and the resulting LTGA trajectory candidates were optimized using a direct method (McConaghy et al. 2003). In some works, patched conic trajectories via CP have been taken as initial guesses for the optimization of LTGA trajectories, the underlying idea of which was that optimal impulsive transfers can be regarded as a limiting case of the fuel-optimal low-thrust transfers with no limit on the thrust level (Okutsu et al. 2006; Vasile & Campagnola 2011). An automated approach was demonstrated to find the number and sequence of swingbys (Englander & Conway 2017). In this approach, two nested optimization algorithms were combined. The outer loop used a genetic algorithm to select the flyby number and sequence while the inner loop solved the corresponding sequence of interplanetary legs using a direct method. Different from the shape-based method and direct method, a practical homotopic method which can be applied to solve LTGA trajectories was proposed (Jiang et al. 2012). However, this method primarily addressed single gravity-assist scenarios, and achieving reliable convergence for multi-gravity assist cases remained challenging due to the large number of unknowns. To deal with this issue, low-thrust trajectories with triple swingbys were divided into three trajectories and solved by a three-step method (Yang et al. 2015). An indirect gradient-based method was also developed to automatically find swingbys under the multi-body dynamics (Olympio 2008).

This work is carried out in three steps. First of all, the determination of number and sequence of swingbys is based on the patched conic trajectories via CP. It is reasonable to apply the results of number and sequence for optimization of LTGA trajectories (Okutsu et al. 2006; Vasile & Campagnola 2011). This method greatly reduces computation time. Second, the initial guesses are globally searched in the design space in two-body dynamics. The first-order necessary conditions for gravity-assist constraints are applied, as derived in the practical homotopic method (Jiang et al. 2012). In addition, the necessary conditions for optimizing initial and final times are derived in this work. An improved cooperative evolutionary

algorithm (ICEA) is used (Lei et al. 2013), where the objective function combines the propellant mass and constraints with penalty factors. Because of the convergence issue for multi-gravity assists in the indirect method, the purpose of this step is not to achieve precise solutions for the MPBVP, but to obtain feasible parameters essential for the subsequent step. Finally, the transfer trajectories are further optimized to achieve higher accuracy. For transfer from Earth to 2020 XL_5, gravitations of Venus, Earth, Mars and Jupiter are considered in order to ensure the accuracy of the transfer trajectory. However, in multi-body dynamics, Euler–Lagrange equations cause sensitivity issues in the indirect method. The costate variables change rapidly over many orders of magnitude during the swingby (Olympio 2008). To address this issue during swingby, instead of solving the whole transfer trajectory directly, a patched-arc model is used. The whole trajectory is segmented into interplanetary trajectory legs governed by gravitation and thrust of the EP system, and coasting planetocentric phases where the spacecraft is only influenced by gravitation. The interplanetary trajectory legs remain outside the planets' sphere of influence (SOI), avoiding the rapid changes in costate variables during swingby.

The structure of this paper is as follows. In Section 2, the three-step approach for designing the low-thrust multi-gravity assist trajectories is introduced, including selecting number and sequence of swingbys, calculating basic parameters of the trajectories, and optimizing the trajectories in multi-body dynamics. Then the three-step approach is applied to design the rendezvous mission to 2020 XL_5. Details of the rendezvous mission are provided in Section 3. The article concludes in Section 4.

2. Methodology

2.1. Determination of Swingby Number and Sequence

In the rendezvous mission to an asteroid, the spacecraft departs from LEO, followed by a series of selected planet swingbys, culminating in the rendezvous with the target asteroid. Below is the search method described in detail. In this work, the delta-v required to launch from LEO is assumed to be supported by the upper stage of a rocket. The departure delta-v is defined by Xu et al. (2007)

$$\Delta v_1 = \sqrt{||\boldsymbol{v}(t_0) - \boldsymbol{v}_E(t_0)||^2 + v_{e\infty}^2} - v_{\mathrm{LEO}}, \tag{1}$$

where $\boldsymbol{v}(t_0)$ and $\boldsymbol{v}_E(t_0)$ are, respectively, the velocity vectors of the spacecraft and Earth in the heliocentric ecliptic reference frame at the departure epoch, and $v_{e\infty} = \sqrt{2\frac{\mu_E}{r_{\mathrm{LEO}}}}$ and $v_{\mathrm{LEO}} = \sqrt{\frac{\mu_E}{r_{\mathrm{LEO}}}}$ are, respectively, the magnitudes of the Earth-escape velocity and actual velocity at the low Earth parking orbit with $r_{\mathrm{LEO}} = 6578.137$ km.

In order to obtain more feasible solutions, deep-space maneuvers (DSMs) are introduced in cases where relative velocities at swingby are not exactly equal (Lei et al. 2017; Gao et al. 2019). For an impulsive maneuver during swingby, the periapsis can be a useful starting point because it is found easily and often close to the optimum solution (Gobetz 1963), which is demonstrated in Figure 1.

When there is a DSM at the periapsis, the angles δ_1, δ_2 and θ can be respectively presented by Gao et al. (2019)

$$\begin{cases} \delta_1 = \arcsin\left(\dfrac{1}{1 + ||\boldsymbol{v}_\infty^-||^2 \frac{r_p}{\mu_P}}\right), \\ \delta_2 = \arcsin\left(\dfrac{1}{1 + ||\boldsymbol{v}_\infty^+||^2 \frac{r_p}{\mu_P}}\right), \\ \cos\theta = \cos(\delta_1 + \delta_2) = \dfrac{||\boldsymbol{v}_\infty^- \cdot \boldsymbol{v}_\infty^+||}{||\boldsymbol{v}_\infty^-||||\boldsymbol{v}_\infty^+||}, \end{cases} \tag{2}$$

where μ_P is the gravitational constant of the planet, r_p is the periapsis radius, and $\boldsymbol{v}_\infty^-$ and $\boldsymbol{v}_\infty^+$ are respectively the hyperbolic excess velocities before and after the DSM. The hyperbolic excess velocities are calculated by $\boldsymbol{v}_\infty^\pm = \boldsymbol{v}(t_{\mathrm{GA}}^\pm) - \boldsymbol{v}_P(t_{\mathrm{GA}})$, where $\boldsymbol{v}_P$ is the velocity vector of the planet in the heliocentric ecliptic reference frame and t_{GA} is the swingby date. When there is no DSM at swingby, the angles have the relationship that $\delta_1 = \delta_2 = \theta/2$. According to Equation (2), the value of r_p can be determined with

$$\theta = \arccos\frac{||\boldsymbol{v}_\infty^- \cdot \boldsymbol{v}_\infty^+||}{||\boldsymbol{v}_\infty^-||||\boldsymbol{v}_\infty^+||} = \arcsin\left(\frac{1}{1 + ||\boldsymbol{v}_\infty^-||^2 \frac{r_p}{\mu_P}}\right) + \arcsin\left(\frac{1}{1 + ||\boldsymbol{v}_\infty^+||^2 \frac{r_p}{\mu_P}}\right). \tag{3}$$

Given a range of r_p, Equation (3) is solved using the bisection method (Gao et al. 2019). The norms of velocity relative to the planet after and before the DSM $v_{sc}^\pm$ can be obtained by applying the method from Gao et al. (2019)

$$v_{sc}^\pm = \sqrt{||\boldsymbol{v}_\infty^\pm||^2 + 2\frac{\mu_P}{r_p}}. \tag{4}$$

Then the DSM impulse Δv_{DSM} is

$$\Delta v_{\mathrm{DSM}} = \sqrt{||\boldsymbol{v}_\infty^+||^2 + 2\frac{\mu_P}{r_p}} - \sqrt{||\boldsymbol{v}_\infty^-||^2 + 2\frac{\mu_P}{r_p}}. \tag{5}$$

Therefore, once r_p is solved, Δv_{DSM} can be obtained.

The rendezvous delta-v is obtained by

$$\Delta v_2 = ||\boldsymbol{v}(t_f) - \boldsymbol{v}_a(t_f)||, \tag{6}$$

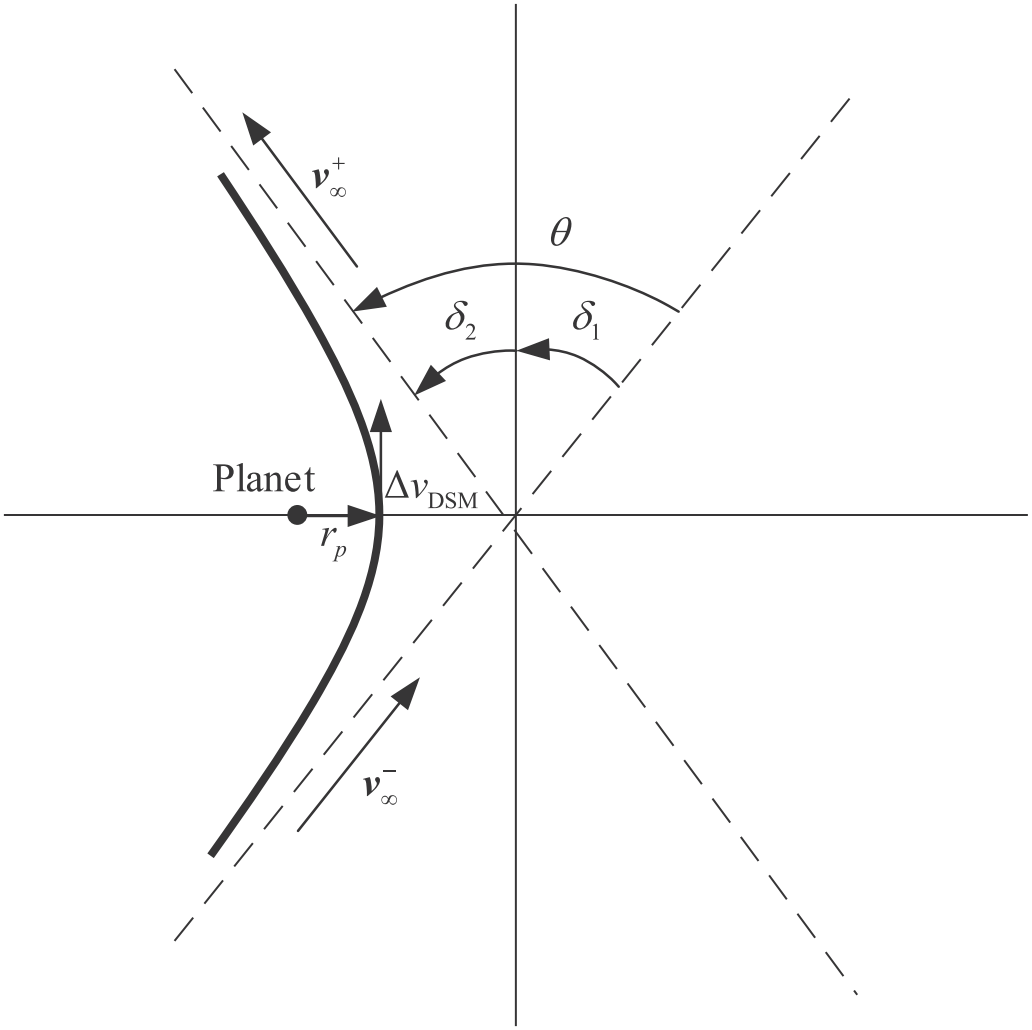

Figure 1. Hyperbolic trajectory during swingby with DSM.

where $\boldsymbol{v}(t_f)$ and $\boldsymbol{v}_a(t_f)$ are respectively the velocity vectors of the spacecraft and target asteroid in heliocentric ecliptic reference frame at rendezvous epoch. The total delta-v budget can be expressed as

$$\Delta v = \Delta v_1 + \Delta v_2 + \sum_{k=1}^{n_0} \Delta v_{\mathrm{DSM}}^{(k)}, \tag{7}$$

where n_0 is the number of swingbys. Usually, during mission planning, constraints should be imposed on the DSM impulse due to the engine's limited thrust capabilities, while constraints should also be placed on the departure delta-v due to the upper stage's limit. However, on the one hand, the optimization process in this procedure focuses on determining the number and sequence of swingbys. On the other hand, the required DSM impulse and excessive departure delta-v are feasible with EP. Therefore, these constraints are ignored in this process. With the total delta-v budget, the impulsive transfer trajectory can be optimized using global optimization algorithm ICEA. Since the swingby altitude is constrained, the objective function is

$$\begin{aligned} J_{\mathrm{sequence}} = \Delta v &+ p_r \sum_{k=1}^{n_0} \max\left(r_{p_{\min},k} - r_{p,k}, 0\right) \\ &+ p_t \max\left(t_f - t_{f_{\max}}, 0\right), \end{aligned} \tag{8}$$

where p_r and p_t are penalty factors, and $t_{f_{\max}}$ is the given maximal flight time for the rendezvous mission. For this case, the decision variables encompass the departure epoch t_0, flight time of spacecraft traveling from Earth to the first swingby planet ΔT_0 and flight times from the k-th swingby planet to the next planet or asteroid ΔT_k ($k = 1, 2,\ldots,n_0$). Then the swingby epochs $t_{\mathrm{GA},k}$ ($k = 1, 2,\ldots,n_0$) and rendezvous epoch t_f can be determined with those decision variables. Subsequently, the

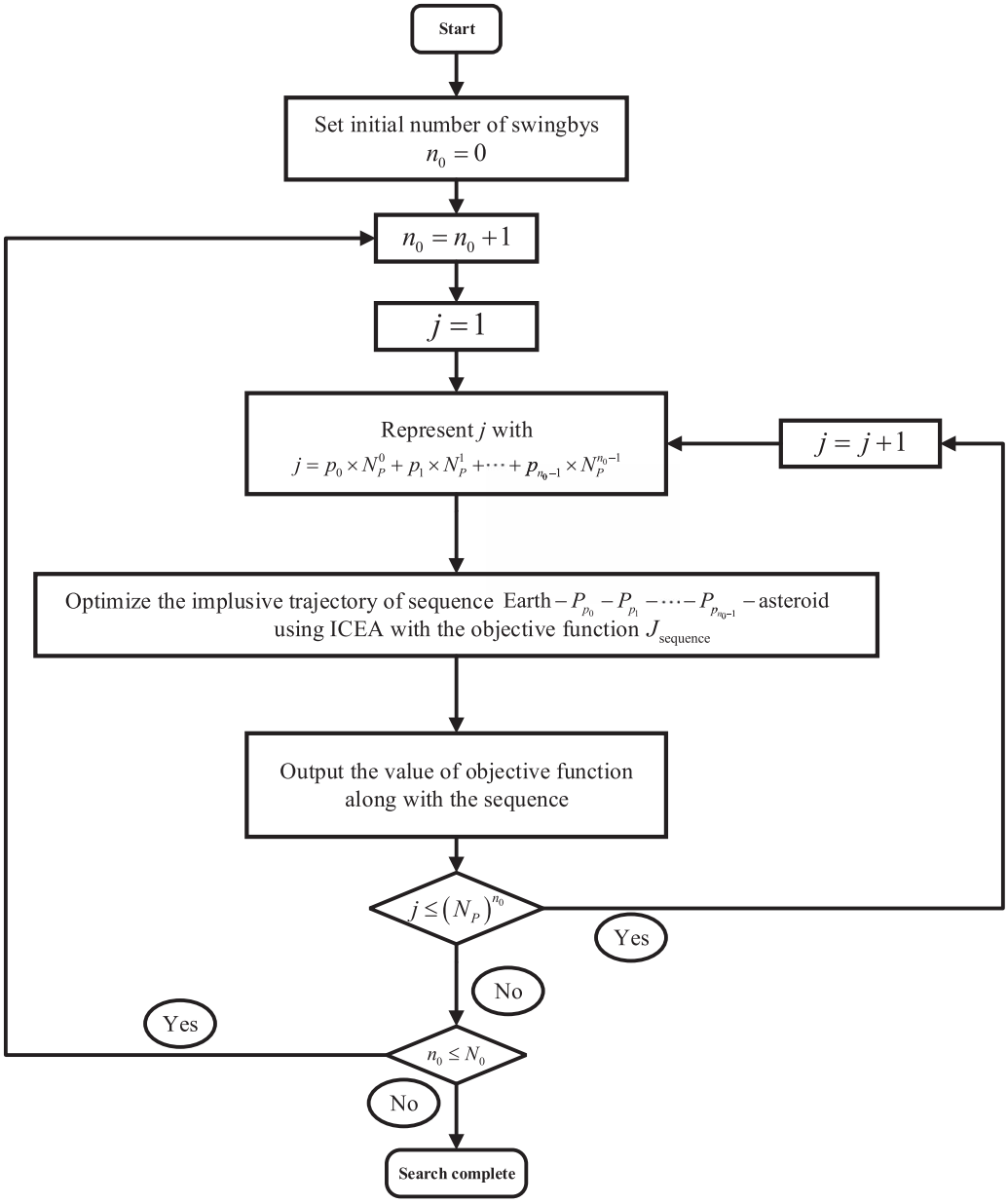

Figure 2. Search algorithm of swingby sequence.

position vectors of the swingby planets are calculated with Keplerian elements.[2] Next, the velocity vectors of the spacecraft at different epochs, including $\boldsymbol{v}(t_0)$, $\boldsymbol{v}(t_f)$ and $\boldsymbol{v}(t_{\text{GA}}^{\pm})$, can be evaluated by solving the Lambert problem (Gooding 1990). Finally, the total delta-v budget is derived using Equations (1), (5), (6) and (7).

The candidate swingby planets available for swingby are denoted as $\{P_0, P_1, \ldots, P_{N_P-1}\}$, where N_P is the count of candidate swingby planets. The maximum number of swingbys is N_0. The approach to search the number and sequence of swingbys is depicted in Figure 2. In this diagram, for a given swingby number n_0, the total number of swingby sequence combinations amounts to $(N_P)^{n_0}$. An integer j between 1 and $(N_P)^{n_0}$ can be represented in base-N_P with $(j)_{\text{dec}} = (p_{n_0-1} \ldots p_1 p_0)_{N_P} = p_{n_0-1} \times N_P^{n_0-1} + \ldots + p_1 \times N_P^1 + p_0 \times N_P^0$. Therefore, every j can be used to represent a transfer sequence for Earth$-P_{p_0} - P_{p_1} - \ldots P_{p_{n_0-1}}-$asteroid. Then the ICEA algorithm is applied to optimize every transfer trajectory corresponding to the sequence Earth$-P_{p_0} - P_{p_1} - \ldots P_{p_{n_0-1}}-$asteroid.

[2] https://ssd.jpl.nasa.gov/planets/approx_pos.html

2.2. Optimization of LTGA Trajectory in Two-body Dynamics

2.2.1. Time-free Fuel-optimal Problem for LTGA Trajectory

In the second step of this work, only the gravitation of the Sun is considered. Most derivations in this optimal problem are based on Jiang et al. (2012). The motion of the spacecraft is governed by the thrust force of the EP system and gravitation of the Sun. The equations of motion (EOM) can be expressed as

$$\begin{cases} \dot{\boldsymbol{r}} &= \boldsymbol{v}, \\ \dot{\boldsymbol{v}} &= -\dfrac{\mu_s}{r^3}\boldsymbol{r} + \dfrac{T_{\max} u}{m}\boldsymbol{\alpha}, \\ \dot{m} &= -\dfrac{T_{\max} u}{I_{sp} g_0}, \end{cases} \tag{9}$$

where $\boldsymbol{r}$ and $\boldsymbol{v}$ respectively denote the position and velocity vectors of the spacecraft in the heliocentric ecliptic reference frame, r is the Euclidean norm of $\boldsymbol{r}$, m is the mass of the spacecraft, μ_s is the gravitational constant of the Sun, $T_{\max}$ and I_{sp} are respectively the maximal thrust and specific impulse of the EP system, g_0 is the gravitational acceleration of Earth at sea level, $u \in [0, 1]$ is the thrust ratio and the unit vector $\boldsymbol{\alpha}$ signifies the direction of thrust. In the optimization of the LTGA trajectory, quantities about length are nondimensionalized by the astronomical unit au = 149,597,870 km. Quantities about time are nondimensionalized by $\sqrt{\mathrm{au}^3/\mu_s}$, where the Sun's gravitational constant is $\mu_s = 1.32712438 \times 10^{11}\,\mathrm{km}^3\,\mathrm{s}^{-2}$. Quantities about mass are nondimensionalized by the spacecraft's initial mass m_0.

Generally, the fuel-optimal problem means maximizing the final mass, or minimizing the fuel consumption, which is defined by

$$J = \frac{T_{\max}}{I_{sp} g_0} \int_{t_0}^{t_f} u dt, \tag{10}$$

where t_0 and t_f are respectively the initial and final times, which are both free. The boundary conditions are as follows

$$\boldsymbol{\Theta}_0 = \begin{cases} \boldsymbol{r}(t_0) - \boldsymbol{r}_E(t_0) \\ \boldsymbol{v}(t_0) - [\boldsymbol{v}_E(t_0) + \boldsymbol{v}_{E\infty}] = 0, \\ m(t_0) - 1 \end{cases} \tag{11}$$

$$\boldsymbol{\Xi}_f = \begin{cases} \boldsymbol{r}(t_f) - \boldsymbol{r}_a(t_f) = 0 \\ \boldsymbol{v}(t_f) - \boldsymbol{v}_a(t_f) = 0 \end{cases}, \tag{12}$$

where $\boldsymbol{r}_E$ is the position vector of Earth, $\boldsymbol{v}_{E\infty}$ is the hyperbolic excess velocity at departure from Earth and $\boldsymbol{r}_a$ is the position vector of the target asteroid in the heliocentric ecliptic reference frame. In addition, for the multi-gravity assist mission, there are also constraints at the swingby points (Jiang et al. 2012)

$$\psi_k = \begin{cases} \boldsymbol{r}(t_{\mathrm{GA},k}) - \boldsymbol{r}_{P,k}(t_{\mathrm{GA},k}) \\ ||\boldsymbol{v}^-_{\infty,k}|| - ||\boldsymbol{v}^+_{\infty,k}|| \end{cases} = 0, \ (k = 1, 2, \ldots, n_0), \tag{13}$$

$$\sigma_k = 1 - r_{p,k}/r_{p_{\min},k} \leqslant 0, \tag{14}$$

where $\boldsymbol{r}_{P,k}$ is the position vector of the k-th swingby planet in the heliocentric ecliptic reference frame. To address both equality and inequality constraints, numerical multipliers $\boldsymbol{\nu}$, $\boldsymbol{\xi}$, $\boldsymbol{\chi}$ and κ are introduced. Moreover, it is well known that in a fuel-optimal problem, the optimal control law has a bang-bang structure, where the discontinuity causes the optimal solution to converge within a limited domain. To overcome this challenge, a numerical continuation method is introduced (Bertrand & Epenoy 2002). There have been various approaches to achieve this (Haberkorn et al. 2004). A homotopic parameter ε is utilized to perturb the performance index (Jiang et al. 2012). For convenience, define

$$G_\varepsilon = \sum_{k=1}^{n_0} (\boldsymbol{\chi}_k \cdot \boldsymbol{\psi}_k + \kappa_k \sigma_k) + \boldsymbol{\nu} \cdot \boldsymbol{\Xi}_f + \boldsymbol{\xi} \cdot \boldsymbol{\Theta}_0. \tag{15}$$

The performance index can be modified as

$$\begin{aligned} J_\varepsilon = \lambda_0 \frac{T_{\max}}{I_{sp} g_0} \Bigg\{ & \sum_{k=1}^{n_0 - 1} \int_{t^+_{\mathrm{GA},k}}^{t^-_{\mathrm{GA},k+1}} [u - \varepsilon u(1 - u)] dt \\ & + \int_{t_0}^{t^-_{\mathrm{GA},1}} [u - \varepsilon u(1 - u)] dt \\ & + \int_{t^+_{\mathrm{GA},n_0}}^{t_f} [u - \varepsilon u(1 - u)] dt \Bigg\} + G_\varepsilon, \end{aligned} \tag{16}$$

where λ_0 is a positive numerical factor applied to normalize the solution. There is a normalization condition of (Jiang et al. 2012)

$$\sqrt{\lambda_0^2 + ||\boldsymbol{\lambda}(t_0)||^2 + \sum_{k=1}^{n_0} (||\boldsymbol{\chi}_k||^2 + \kappa_k^2)} = 1, \tag{17}$$

where $\boldsymbol{\lambda} \triangleq (\boldsymbol{\lambda}_r; \boldsymbol{\lambda}_v; \lambda_m)$ is the costate vector. When the parameter $\varepsilon = 1$, the performance index is identical to that of the energy-optimal problem, which is easier to solve because of its control continuity. By the use of Pontryagin's Maximum Principle (PMP), this problem can be transformed into an MPBVP. The corresponding Hamiltonian is constructed (Jiang et al. 2012)

$$\begin{aligned} H_\varepsilon = & \boldsymbol{\lambda}_r \cdot \boldsymbol{v} + \boldsymbol{\lambda}_v \cdot \left(-\frac{\mu_s}{r^3}\boldsymbol{r} + \frac{T_{\max} u}{m}\boldsymbol{\alpha} \right) - \lambda_m \frac{T_{\max} u}{I_{sp} g_0} \\ & + \lambda_0 \frac{T_{\max}}{I_{sp} g_0} [u - \varepsilon u(1 - u)]. \end{aligned} \tag{18}$$

According to PMP, the optimal thrust direction and magnitude, which minimize the Hamiltonian, are determined by

Jiang et al. (2012)

$$\boldsymbol{\alpha} = -\frac{\boldsymbol{\lambda}_v}{||\boldsymbol{\lambda}_v||}, \tag{19}$$

$$u = \begin{cases} 0 & \text{if SF} > \varepsilon \\ 1 & \text{if SF} < -\varepsilon \\ \dfrac{1}{2} - \dfrac{\text{SF}}{2\varepsilon} & \text{if } |\text{SF}| \leqslant \varepsilon \end{cases}, \tag{20}$$

where SF is the switching function, which takes the form

$$\text{SF} = 1 - \frac{I_{sp} g_0 ||\boldsymbol{\lambda}_v||}{\lambda_0 m} - \frac{\lambda_m}{\lambda_0}. \tag{21}$$

Substituting the optimal control law presented by Equation (19) into the Hamiltonian function, the differential equations governing the costate variables, often called Euler–Lagrange equations, can be derived

$$\begin{cases} \dot{\boldsymbol{\lambda}}_{\boldsymbol{r}} &= \mu_s \left(\dfrac{\boldsymbol{\lambda}_v}{r^3} - \dfrac{3\boldsymbol{\lambda}_v \cdot \boldsymbol{r}}{r^5} \boldsymbol{r} \right) \\ \dot{\boldsymbol{\lambda}}_{\boldsymbol{v}} &= -\boldsymbol{\lambda}_{\boldsymbol{r}}, \\ \dot{\lambda}_m &= -\dfrac{T_{\max} u}{m^2} ||\boldsymbol{\lambda}_v||. \end{cases} \tag{22}$$

The transversality conditions for swingbys are (Jiang et al. 2012)

$$\boldsymbol{\lambda}_{\boldsymbol{r}}(t^+_{\text{GA},k}) = \boldsymbol{\lambda}_{\boldsymbol{r}}(t^-_{\text{GA},k}) - \boldsymbol{\chi}_{1\sim3,k}, \tag{23}$$

$$\boldsymbol{\lambda}_{\boldsymbol{v}}(t^+_{\text{GA},k}) = \boldsymbol{\chi}_{4,k} \boldsymbol{i}^+_k + \frac{1}{r_{p_{\min},k}} \kappa_k B, \tag{24}$$

$$\boldsymbol{\varphi}_{1\sim3,k} = \boldsymbol{\lambda}_{\boldsymbol{v}}(t^-_{\text{GA},k}) - \boldsymbol{\chi}_{4,k} \boldsymbol{i}^-_k + \frac{1}{r_{p_{\min},k}} \kappa_k \boldsymbol{A} = 0, \tag{25}$$

$$\begin{aligned} \varphi_{4,k} &= H_\varepsilon(t^-_{\text{GA},k}) - H_\varepsilon(t^+_{\text{GA},k}) - \boldsymbol{\chi}_{1\sim3,k} \cdot \boldsymbol{v}_{P,k}(t_{\text{GA},k}) \\ &+ \boldsymbol{\chi}_{4,k}(\boldsymbol{i}^+_k - \boldsymbol{i}^-_k) \cdot \boldsymbol{a}_{P,k}(t_{\text{GA},k}) - \frac{1}{r_{p_{\min},k}} \kappa_k \boldsymbol{C} = 0, \end{aligned} \tag{26}$$

where $\boldsymbol{i}^\pm_k = \boldsymbol{v}^\pm_{\infty,k} / ||\boldsymbol{v}^\pm_{\infty,k}||$ is the unit vector of $\boldsymbol{v}^\pm_{\infty,k}$, and $\boldsymbol{a}_{P,k}$ is the acceleration vector of the k-th swingby planet. Equations (23) and (24) are used to update the position and velocity costate vectors. Detailed information for $\boldsymbol{A}$, $\boldsymbol{B}$ and $\boldsymbol{C}$ can be found in Jiang et al. (2012), and they have the forms

$$\boldsymbol{A} = \frac{r_{p,k}}{||\boldsymbol{v}^-_{\infty,k}||} \left[\frac{1}{4\sin^2\theta/2(1-\sin\theta/2)} (\boldsymbol{i}^+_k - \cos\theta \boldsymbol{i}^-_k) - \boldsymbol{i}^-_k \right], \tag{27}$$

$$\boldsymbol{B} = \frac{r_{p,k}}{||\boldsymbol{v}^+_{\infty,k}||} \left[\frac{1}{4\sin^2\theta/2(1-\sin\theta/2)} (\boldsymbol{i}^-_k - \cos\theta \boldsymbol{i}^+_k) - \boldsymbol{i}^+_k \right], \tag{28}$$

$$\begin{aligned} \boldsymbol{C} = r_{p,k} \Bigg\{ &- \frac{1}{4\sin^2\theta/2(1-\sin\theta/2)} \left[\frac{1}{||\boldsymbol{v}^+_{\infty,k}||} (\boldsymbol{i}^-_k - \cos\theta \boldsymbol{i}^+_k) \right. \\ &\left. + \frac{1}{||\boldsymbol{v}^-_{\infty,k}||} (\boldsymbol{i}^+_k - \cos\theta \boldsymbol{i}^-_k) \right] + \frac{\boldsymbol{i}^+_k}{||\boldsymbol{v}^+_{\infty,k}||} + \frac{\boldsymbol{i}^-_k}{||\boldsymbol{v}^-_{\infty,k}||} \Bigg\} \\ \cdot \boldsymbol{a}_{P,k}(t_{\text{GA},k}). \end{aligned} \tag{29}$$

In addition, the complementary slackness conditions due to the inequality constraints are (Jiang et al. 2012)

$$\kappa_k \sigma_k = 0, \quad \kappa_k \geqslant 0. \tag{30}$$

In Jiang et al. (2012), the initial time and final time are fixed. In contrast, the approach in this paper allows for flexibility in both initial and final times. For the time-free problem, the first differential boundary conditions are given by Hull (2013)

$$H(t_0) = \frac{\partial G_\varepsilon}{\partial t_0}, \quad \boldsymbol{\lambda}(t_0) = -\left[\frac{\partial G_\varepsilon}{\partial \boldsymbol{x}(t_0)} \right]^{\mathrm{T}}, \tag{31}$$

$$H(t_f) = -\frac{\partial G_\varepsilon}{\partial t_f}, \quad \boldsymbol{\lambda}(t_f) = \left[\frac{\partial G_\varepsilon}{\partial \boldsymbol{x}(t_f)} \right]^{\mathrm{T}}, \tag{32}$$

where $\boldsymbol{x} \triangleq (\boldsymbol{r}; \boldsymbol{v}; m)$. Therefore, the transversality conditions are obtained as

$$\varphi_{1,f} = H_\varepsilon(t_0) - \boldsymbol{\lambda}_{\boldsymbol{r}}(t_0) \cdot \boldsymbol{v}_E(t_0) - \boldsymbol{\lambda}_{\boldsymbol{v}}(t_0) \cdot \boldsymbol{a}_E(t_0) = 0, \tag{33}$$

$$\varphi_{2,f} = H_\varepsilon(t_f) - \boldsymbol{\lambda}_{\boldsymbol{r}}(t_f) \cdot \boldsymbol{v}_a(t_f) - \boldsymbol{\lambda}_{\boldsymbol{v}}(t_f) \cdot \boldsymbol{a}_a(t_f) = 0, \tag{34}$$

$$\lambda_m(t_f) = 0. \tag{35}$$

where $\boldsymbol{a}_a$ is the acceleration vector of the target asteroid in the heliocentric ecliptic reference frame. For the energy-optimal problem ($\varepsilon = 1$), the differential equations expressed by Equations (9) and (22) are numerically integrated using the classic eighth-order Runge–Kutta integrator with a seventh order for automatic step-size control, i.e., RKF7(8) (Fehlberg 1968). However, as the homotopic parameter ε approaches 0, the right-hand sides of ordinary differential equations (ODEs) experience abrupt variations around switching points. To ensure the accuracy of integration with RKF7(8), the bisection method is used to detect the switching points (Martinon & Gergaud 2010; Zhang et al. 2015).

For this MPBVP at $\varepsilon = 1$, there are $10 + 9n_0$ unknowns in total, including initial and final times t_0, t_f, the positive numerical factor λ_0, seven initial values of costate vector $\boldsymbol{\lambda}(t_0)$, 3D gravity-assist impulse vectors $\Delta\boldsymbol{v}_{G,k} = \boldsymbol{v}^+_{\infty,k} - \boldsymbol{v}^-_{\infty,k}$ ($k = 1, 2, \ldots, n_0$), swingby dates $t_{\text{GA},k}$, 4D numerical Lagrange multipliers $\boldsymbol{\chi}_k$ and 1D Lagrange multipliers κ_k. Meanwhile, there are $10 + 9n_0$ equations as well, consisting of the 6D Equation (12), the 1D Equation (33), the 1D Equation (34), the 1D Equation (35), the 4D Equation (13) $\boldsymbol{\psi}_k$, the 1D Equation (30) with the application of inequality Equation (14) σ_k, the 3D Equation (25) $\boldsymbol{\varphi}_{1\sim3,k}$, the 1D Equation (26) $\varphi_{4,k}$ and the normalization condition Equation (17).

2.2.2. Global Search with ICEA Algorithm

The main purpose of the second step is to obtain feasible basic parameters, which can be applied in the optimization of LTGA trajectories in the next step. These basic parameters include initial and final times t_0 and t_f respectively, swingby dates $t_{\text{GA},k}$, launch $\boldsymbol{v}_{E\infty}$, hyperbolic excess velocities $\boldsymbol{v}^\pm_{\infty,k}$ and

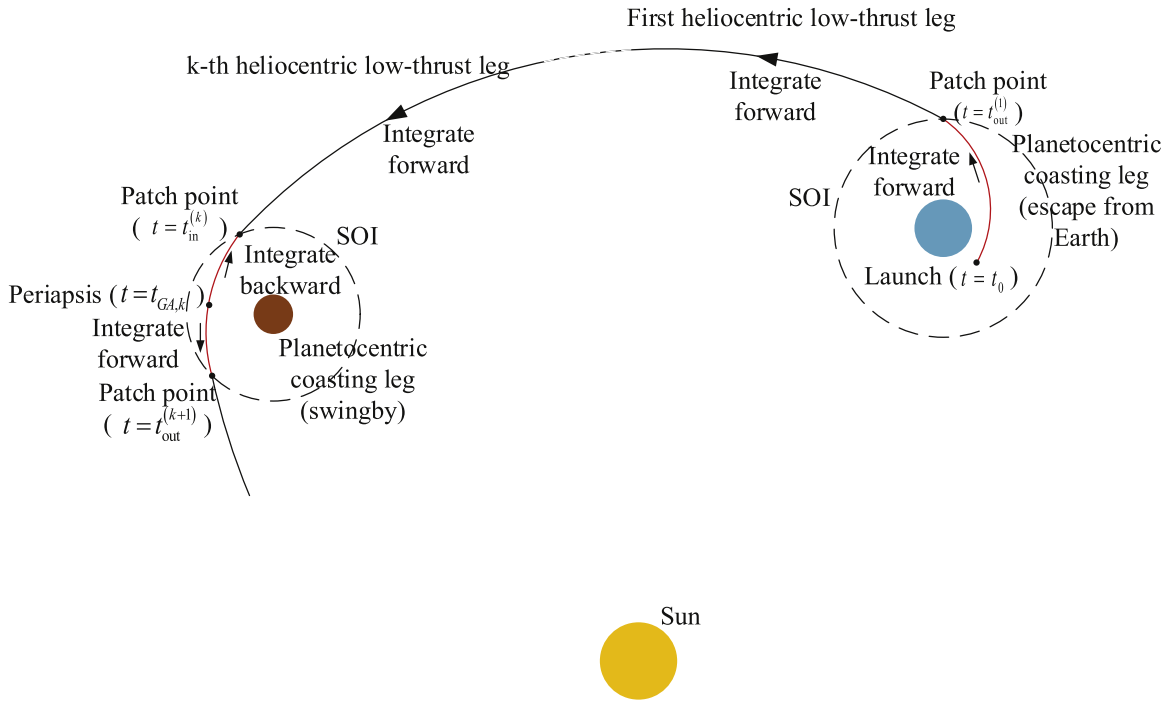

Figure 3. Scheme of patched-arc model.

periapsis radius $r_{p,k}$ at swingbys. Because it would be difficult to solve the MPBVP directly, a global optimization method is employed to obtain these parameters. Accurate solutions are not required in this search. To reduce the computation time, the control law based on the energy-optimal problem ($\varepsilon = 1$) is utilized to search the parameters. With normalization condition Equation (17), the search space can be transformed from an unbounded space into a hypersphere (Jiang et al. 2012). The $8 + 5n_0$ variables λ_0, $\boldsymbol{\lambda}(t_0)$, $\boldsymbol{\chi}_k$ and κ_k are normalized with $7 + 5n_0$ angle variables $\boldsymbol{\beta}$. In addition to the variables involved in the MPBVP, launch $\boldsymbol{v}_{E\infty}$ is considered a decision variable in the global optimization process. Meanwhile, as the problem is constrained, penalty factors are introduced to turn it into an unconstrained one. The objective function is expressed as

$$f(\boldsymbol{\gamma}) = m_p + p_f||\Gamma|| + p_t \max(t_f - t_{f_{\max}}, 0), \tag{36}$$

where $\boldsymbol{\gamma} \triangleq (\boldsymbol{\beta}; t_0; \Delta T_0; \Delta T_k; \boldsymbol{v}_{E\infty}; \Delta \boldsymbol{v}_{G,k})$, $\boldsymbol{\Gamma} \triangleq [\boldsymbol{\Xi}_f; \psi_k; \kappa_k \sigma_k; \varphi_k; \varphi_f; \lambda_m(t_f)]$. In this search, the penalty factors are $p_f = 1000$ and $p_t = 1000$.

2.3. Design of LTGA Trajectory in Multi-body Dynamics

2.3.1. Time-fixed Fuel-optimal Problem Without Swingby in Multi-body Dynamics

In the third step, the third-body perturbations of the planets in the solar system are considered. The problem without swingby is stated in multi-body dynamics here. Given that the orbital elements provided by the Minor Planet Center (MPC) are heliocentric, the EOM are described in the heliocentric ecliptic reference frame. Most derivations are identical to those in a time-free fuel-optimal problem in two-body dynamics, with the exception of the EOM and Euler–Lagrange equations. The motion of the spacecraft is governed by the thrust force of the EP system, as well as the gravitations of Sun, Earth and other planets in the solar system. The EOM can be expressed as

$$\begin{cases} \dot{\boldsymbol{r}} = \boldsymbol{v}, \\ \dot{\boldsymbol{v}} = -\dfrac{\mu_s}{r^3}\boldsymbol{r} - \displaystyle\sum_{i=1}^{10} \mu_i \left(\frac{\boldsymbol{r} - \boldsymbol{r}_i}{||\boldsymbol{r} - \boldsymbol{r}_i||^3} + \frac{\boldsymbol{r}_i}{||\boldsymbol{r}_i||^3} \right) + \dfrac{T_{\max} u}{m}\boldsymbol{\alpha}, \\ \dot{m} = -\dfrac{T_{\max} u}{I_{sp} g_0}, \end{cases} \tag{37}$$

Table 1
Heliocentric Orbital Elements of 2020 XL_5

Epoch (MJD)	59649.0
Semimajor axis, a (au)	1.0006928
Eccentricity, e	0.3871117
Inclination, i (Deg)	13.84744
Longitude of ascending node, Ω (Deg)	153.59764
Argument of perihelion, ω (Deg)	87.98465
Mean anomaly, M (Deg)	4.6601

Table 2
Keplerian Elements of the Swingby Planets

	Venus	Earth/Moon Barycenter	Mars
Epoch (MJD)	51,544.5	51,544.5	51,544.5
Semimajor axis, a_0 (au)	0.72332102	1.00000018	1.52371243
$\dot{a}$ (au/Century)	−0.00000026	−0.00000003	0.00000097
Eccentricity, e_0 (Rad)	0.00676399	0.01673163	0.09336511
$\dot{e}$ (Rad/Century)	−0.00005107	-0.00003661	0.00009149
Inclination, I_0 (Deg)	3.39777545	−0.00054346	1.85181869
$\dot{I}$ (Deg/Century)	0.00043494	−0.01337178	−0.00724757
Mean longitude, L_0 (Deg)	181.97970850	100.46691572	−4.56813164
$\dot{L}$ (Deg/Century)	58,517.81560260	35,999.37306329	19,140.29934243
Longitude of perihelion, ϖ_0 (Deg)	131.76755713	102.93005885	−23.91744784
$\dot{\varpi}$ (Deg/Century)	0.05679648	0.31795260	0.45223625
Longitude of the ascending node, Ω_0 (Deg)	76.67261496	−5.11260389	49.71320984
$\dot{\Omega}$ (Deg/Century)	−0.27274174	−0.24123856	−0.26852431

Table 3
Candidate Swingby Sequences and Performances

Transfer sequence	n_0	Δv (km s^{-1})	Transfer sequence	n_0	Δv (km s^{-1})
E-2020 XL_5	0	10.33	E-V-E-V-2020 XL_5	3	6.31
E-E-V-E-V-2020 XL_5	4	7.00	E-E-V-2020 XL_5	2	7.95
E-V-2020 XL_5	1	7.97	E-E-E-V-E-2020 XL_5	4	8.27
E-V-M-V-2020 XL_5	3	8.35	E-V-V-2020 XL_5	2	8.39
E-V-E-2020 XL_5	2	8.58	E-E-V-M-V-2020 XL_5	4	8.76
E-E-V-E-2020 XL_5	3	8.88			

Table 4
Parameters of the Impulsive Transfer Trajectory Corresponding to the Earth–Venus–Earth–Venus-2020 XL_5 Swingby Sequence

Launch date (m/d/y)	1/6/2025
Venus' first swingby date (m/d/y)	3/26/2025
Venus' first swingby altitude (km)	5025.7
Earth's swingby date (m/d/y)	2/6/2026
Earth's swingby altitude (km)	43,125.2
Venus' second swingby date (m/d/y)	1/26/2027
Venus' second swingby altitude (km)	215.4
Rendezvous date (m/d/y)	12/12/2027
Departure delta-v (km s^{-1})	4.52
DSM at Venus' first swingby (km s^{-1})	1.18×10^{-2}
DSM at Earth's swingby (km s^{-1})	4.54×10^{-3}
DSM at Venus' second swingby (km s^{-1})	2.19×10^{-2}
Rendezvous delta-v (km s^{-1})	1.69
Total delta-v (km s^{-1})	6.26
Flight time (days)	1069.42
Propellant mass ratio (m_p/m_0)	44.51%

where μ_i ($i = 1, 2,\ldots,8$ for eight planets, $i = 9$ for Pluto and $i = 10$ for the Moon) is the gravitational constant of the corresponding celestial body, and $\boldsymbol{r}_i$ is the position vector of the corresponding celestial body. In this step, the states of planets are also determined using the JPL ephemeris DE 421. The boundary conditions are

$$\boldsymbol{r}(t_0^*) = \boldsymbol{r}_0^*, \quad \boldsymbol{v}(t_0^*) = \boldsymbol{v}_0^*, \quad m(t_0^*) = m_0^*, \tag{38}$$

$$\boldsymbol{r}(t_f^*) = \boldsymbol{r}_f^*, \quad \boldsymbol{v}(t_f^*) = \boldsymbol{v}_f^*. \tag{39}$$

For the optimization of low-thrust trajectory between planets, there are no additional intermediate constraints. Applying the homotopic parameter ε, the performance index and corresponding Hamiltonian are as follows

$$J_\varepsilon^* = \lambda_0 \frac{T_{\max}}{I_{sp} g_0} \int_{t_0^*}^{t_f^*} [u - \varepsilon u(1-u)]\, dt, \tag{40}$$

$$\begin{aligned} H_\varepsilon^* &= \boldsymbol{\lambda_r} \cdot \boldsymbol{v} + \boldsymbol{\lambda_v} \\ &\cdot \left[-\frac{\mu_s}{r^3}\boldsymbol{r} - \sum_{i=1}^{10} \mu_i \left(\frac{\boldsymbol{r} - \boldsymbol{r}_i}{\| \boldsymbol{r} - \boldsymbol{r}_i \|^3} + \frac{\boldsymbol{r}_i}{r_i^3} \right) + \frac{T_{\max} u}{m} \boldsymbol{\alpha} \right] \\ &- \lambda_m \frac{T_{\max} u}{I_{sp} g_0} + \lambda_0 \frac{T_{\max}}{I_{sp} g_0} [u - \varepsilon u(1-u)]. \end{aligned} \tag{41}$$

The optimal thrust magnitude and direction are the same with those in two-body dynamics, which are determined by Equations (19), (20) and (21). Combining the optimal control law and the Hamiltonian function, the Euler–Lagrange

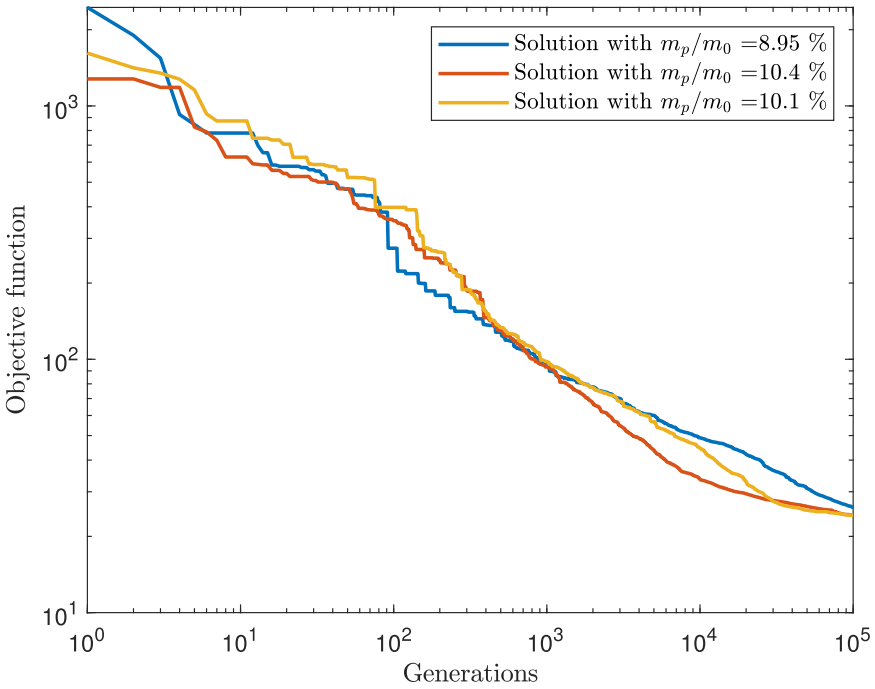

Figure 4. Convergence curves of the solutions.

Table 5
Basic Parameters for Optimization of LTGA Trajectory Corresponding to the Earth–Venus–Earth–Venus-2020 XL_5 Swingby Sequence

Launch date (m/d/y)	1/3/2025
Launch $\boldsymbol{v}_{E\infty}$ (km s^{-1})	[5.60, 2.37, 1.52]
Norm of launch $\boldsymbol{v}_{E\infty}$ (km s^{-1})	6.27
Venus' first swingby date (m/d/y)	3/21/2025
Venus' first swingby altitude (km)	2969.6
$\boldsymbol{v}^-_{\infty,1}$ (km s^{-1})	[12.25, 2.04, 0.22]
$\boldsymbol{v}^+_{\infty,1}$ (km s^{-1})	[12.14, − 2.32, 1.96]
Earth's swingby date (m/d/y)	2/3/2026
Earth's swingby altitude (km)	33 578.8
$\boldsymbol{v}^-_{\infty,2}$ (km s^{-1})	[10.35, − 6.65, 2.32]
$\boldsymbol{v}^+_{\infty,2}$ (km s^{-1})	[10.87, − 5.49, 3.11]
Venus' second swingby date (m/d/y)	1/21/2027
Venus' second swingby altitude (km)	845.6
$\boldsymbol{v}^-_{\infty,3}$ (km s^{-1})	[13.79, − 1.59, 2.43]
$\boldsymbol{v}^+_{\infty,3}$ (km s^{-1})	[11.88, − 2.97, 7.27]
Rendezvous date (m/d/y)	3/5/2028
Flight time (days)	1156.84

equations in multi-body dynamics are described as

$$\begin{cases} \dot{\boldsymbol{\lambda}}_{\boldsymbol{r}} = \mu_s\left(\dfrac{\boldsymbol{\lambda}_{\boldsymbol{v}}}{r^3} - \dfrac{3\boldsymbol{\lambda}_{\boldsymbol{v}}\cdot\boldsymbol{r}}{r^5}\boldsymbol{r}\right) + \sum_{i=1}^{10}\mu_i\left[\dfrac{\boldsymbol{\lambda}_{\boldsymbol{v}}}{||\boldsymbol{r}-\boldsymbol{r}_i||^3} - \dfrac{3\boldsymbol{\lambda}_{\boldsymbol{v}}\cdot(\boldsymbol{r}-\boldsymbol{r}_i)}{||\boldsymbol{r}-\boldsymbol{r}_i||^5}(\boldsymbol{r}-\boldsymbol{r}_i)\right], \\ \dot{\boldsymbol{\lambda}}_{\boldsymbol{v}} = -\boldsymbol{\lambda}_{\boldsymbol{r}}, \\ \dot{\lambda}_m = -\dfrac{T_{\max}u}{m^2}||\boldsymbol{\lambda}_{\boldsymbol{v}}||. \end{cases} \tag{42}$$

Table 6
Orbital Elements of Parking Orbit at Launch in Earth-centered Inertial Frame, Date and Velocity Vector at the Boundary of SOI in Earth-centered Ecliptic Reference Frame

Epoch (MJD)	60,678.85
Semimajor axis, a (km)	6578.137
Eccentricity, e	0
Inclination, i (Deg)	28.5
Longitude of ascending node, Ω (Deg)	327.904
Argument of perigee, ω (Deg)	284.087
Mean anomaly, M (Deg)	0
Departure delta-v, Δv_1 (km s^{-1})	4.88
Date leaving Earth's SOI (m/d/y)	1/5/2025
Velocity vector leaving Earth's SOI (km s^{-1})	[5.66, 2.40, 1.54]

In the third step, the initial time and final time are fixed. There is only one transversality condition on the mass costate shown in Equation (35). The normalization condition is modified as

$$\sqrt{\lambda_0^2 + ||\boldsymbol{\lambda}(t_0^*)||^2} = 1. \tag{43}$$

For this TPBVP at $\varepsilon = 1$, by the use of normalization condition in Equation (43), there are seven unknowns, i.e., the seven angle variables transformed from λ_0 and $\boldsymbol{\lambda}(t_0)$. There are seven constraints including the boundary conditions in 6D in Equation (39) and the transversality condition in Equation (35). When the homotopic parameter $\varepsilon < 1$, the positive numerical factor λ_0 is held constant at the value

Table 7
Orbital Elements of Hyperbolic Trajectories at Periapsis, Dates and Velocity Vectors at the Boundary of SOI in Planetocentric Ecliptic Reference Frame

	Venus' First Swingby	Earth's Swingby	Venus' Second Swingby
Epoch (MJD)	60,755.72	61,074.51	61,426.77
Semimajor axis, a (km)	2072.93	2523.43	1601.83
Eccentricity, e	5.352	16.834	5.306
Inclination, i (Deg)	157.652	34.353	107.114
Longitude of ascending node, Ω (Deg)	11.892	311.230	356.494
Argument of periapsis, ω (Deg)	283.564	292.636	291.437
True anomaly, f (Deg)	0	0	0
Date entering SOI (m/d/y)	3/21/2025	2/2/2026	1/21/2027
Velocity vector entering SOI (km s^{-1})	[12.40, 2.03, 0.23]	[10.42, −6.69, 2.34]	[13.96, −1.63, 2.50]
Date leaving SOI (m/d/y)	3/22/2025	2/4/2026	1/22/2027
Velocity vector leaving SOI (km s^{-1})	[12.19, −2.32, 1.97]	[10.90, −5.51, 3.12]	[11.91, −2.98, 7.29]

Table 8
Parameters of LTGA Trajectory Corresponding to the Earth–Venus–Earth–Venus-2020 XL_5 Swingby Sequence

Departure date (m/d/y)	1/3/2025
Norm of $\boldsymbol{V}_E(t_{\text{out}}^{(1)})$ (km s^{-1})	6.34
Propellant mass of first leg (kg)	4.4
Venus' first swingby date at periapsis (m/d/y)	3/21/2025
Norm of velocity vector at the boundary of SOI (km s^{-1})	12.56
Propellant mass of second leg (kg)	4.7
Earth's swingby date at periapsis (m/d/y)	2/3/2026
Norm of velocity vector at the boundary of SOI (km s^{-1})	12.60
Propellant mass of third leg (kg)	22.3
Venus' second swingby date at periapsis (m/d/y)	1/21/2027
Norm of velocity vector at the boundary of SOI (km s^{-1})	14.28
Propellant mass of fourth leg (kg)	40.8
Rendezvous date (m/d/y)	3/5/2028
Flight time (days)	1156.84
Total propellant mass (kg)	72.2
Total propellant mass ratio (%)	9.03

obtained in the energy-optimal problem. There are seven unknowns at $\varepsilon < 1$, i.e., the initial values of costate vector $\boldsymbol{\lambda}(t_0)$. The normalization condition is not applicable at $\varepsilon < 1$. Compared with the MPBVP for low-thrust multi-gravity assists, a good initial guess of TPBVP is easier to obtain using global optimization. Thus, a numerical method for solving nonlinear equations is applied for this problem to attain precise transfer trajectories. Here, the ICEA algorithm is utilized to search for an initial guess of the energy-optimal problem. The objective function is expressed as

$$f(\boldsymbol{\beta}^*) = p_f ||\Gamma^*||, \tag{44}$$

where $\boldsymbol{\beta}^*$ is the seven angle variables transformed from λ_0 and $\boldsymbol{\lambda}(t_0)$ according to the normalization condition, and $\boldsymbol{\Gamma}^*$ consists of the boundary condition in Equation (39) and the transversality condition in Equation (35). In this paper, a hybrid solver in the GNU Scientific Library (GSL) is used to solve the TPBVP (Powell 1970). The steps of solving the fuel-optimal problem can be summarized as (Jiang et al. 2012):

1. Apply the ICEA algorithm to search for approximate solutions of the normalized costate $[\boldsymbol{\lambda}_{\boldsymbol{r}}(t_0); \boldsymbol{\lambda}_{\boldsymbol{v}}(t_0); \lambda_m(t_0)]$ and positive numerical factor λ_0 to the energy-optimal problem, i.e., $\varepsilon = 1$. The integrator is RKF7(8).
2. Take the approximate normalized solution of step 1 as an initial guess to solve the accurate solution of the energy-optimal problem. The integrator is RKF7(8), and the solver is a hybrid solver in GSL. Go back to step 1 if it does not converge.
3. Fix the positive factor λ_0, and decrease the parameter ε gradually until zero. Solve the new problem using the previous solution as an initial guess. The integrator is RKF7(8) combined with the bisection method to detect the switching points. If it does not converge, shorten the decreasing step and try it again.
4. Output the solutions of the fuel-optimal problem.

2.3.2. *Patched-arc Model for Optimization of LTGA Trajectory*

The patched-arc model is often used for interplanetary missions (Melbourne & Sauer 1965; Pierson & Kluever 1994). Swingby planets are often seen as massless, and the swingbys are considered as instantaneous events (Johnson 1969). However, when considering multi-body dynamics, this assumption is not adequate. To deal with the rapid changes of costate variables during a swingby, the hyperbolic trajectory within the planet's SOI remains unpowered, only subject to gravitation. The SOI is applied to place the limit between each low-thrust leg. Once the low-thrust legs remain outside the SOI, there are no rapid changes in costate variables anymore. The radius of SOI of a planet P is calculated by Bate et al. (2020)

$$r_{\text{SOI}} = a_P \left(\frac{m_P}{M_s}\right)^{\frac{2}{5}}, \tag{45}$$

where a_P is the semimajor axis of the orbit of planet P, and m_P and M_s are the masses of planet P and the Sun respectively. For the kth low-thrust leg starting from the boundary of the $k-1$th celestial body's SOI to the boundary of the kth celestial body's SOI, the boundary conditions are expressed as

$$\begin{aligned} \boldsymbol{r}(t_{\text{out}}^{(k)}) &= \boldsymbol{r}_{P,k-1}(t_{\text{out}}^{(k)}) + \boldsymbol{R}_{P,k-1}(t_{\text{out}}^{(k)}), \\ \boldsymbol{v}(t_{\text{out}}^{(k)}) &= \boldsymbol{v}_{P,k-1}(t_{\text{out}}^{(k)}) + \boldsymbol{V}_{P,k-1}(t_{\text{out}}^{(k)}), \\ m(t_{\text{out}}^{(k)}) &= m(t_{\text{in}}^{(k-1)}), \end{aligned} \tag{46}$$

$$\begin{aligned} \boldsymbol{r}(t_{\text{in}}^{(k)}) &= \boldsymbol{r}_{P,k}(t_{\text{in}}^{(k)}) + \boldsymbol{R}_{P,k}(t_{\text{in}}^{(k)}), \\ \boldsymbol{v}(t_{\text{in}}^{(k)}) &= \boldsymbol{v}_{P,k}(t_{\text{in}}^{(k)}) + \boldsymbol{V}_{P,k}(t_{\text{in}}^{(k)}). \end{aligned} \tag{47}$$

In the equations above, the superscript (k) denotes the kth low-thrust leg, $t_{\text{out}}^{(k)}$ is the date when the spacecraft leaves the $k-1$th celestial body's SOI, $t_{\text{in}}^{(k)}$ is the date when the spacecraft enters the kth celestial body's SOI, and $\boldsymbol{R}_{P,k}$ and $\boldsymbol{V}_{P,k}$ are respectively the position and velocity vectors of the spacecraft in the planetocentric ecliptic reference frame. The 0th celestial body is Earth. Define $m(t_{\text{in}}^{(0)}) = 1$. Because the n_0+1th celestial body is the target asteroid 2020 XL_5, there are $t_{\text{in}}^{(n_0+1)} = t_f$ and $\boldsymbol{R}_{P,n_0+1}(t_{\text{in}}^{(n_0+1)}) = \boldsymbol{V}_{P,n_0+1}(t_{\text{in}}^{(n_0+1)}) = 0$.

The position and velocity vectors of a spacecraft at the boundary of Earth's SOI $\boldsymbol{R}_{P,0}(t_{\text{out}}^{(1)})$, $\boldsymbol{V}_{P,0}(t_{\text{out}}^{(1)})$ and the corresponding date $t_{\text{out}}^{(1)}$ are determined by integrating the state of the spacecraft from the parking orbit after the launch supported by the upper stage of the rocket at $t = t_0$. The orbital elements of the parking orbit are derived using the launch $\boldsymbol{v}_{E\infty}$. In addition, the orbital elements of the parking orbit are expressed in the Earth-centered inertial frame. For the parking orbit, eccentricity e_{park} and semimajor axis a_{park} are both known, and the mean anomaly is set as $M = 0$, which is the perigee. There is a minimal admissible inclination i_{min} for given $\boldsymbol{v}_{E\infty}$. When the required inclination of parking orbit i_0 is larger than i_{min}, the inclination is $i_{\text{park}} = i_0$. Otherwise the inclination is $i_{\text{park}} = i_{\text{min}}$. The expressions of i_{min}, longitude of ascending node Ω and argument of perigee ω are shown in the Appendix. With the orbital elements and departure delta-v given, $t_{\text{out}}^{(1)}$, $\boldsymbol{R}_E^{\text{ECI}}(t_{\text{out}}^{(1)})$ and $\boldsymbol{V}_E^{\text{ECI}}(t_{\text{out}}^{(1)})$ in the Earth-centered inertial frame are obtained by integrating the EOM of an unpowered spacecraft until $||\boldsymbol{R}_E(t)|| \geqslant r_{\text{SOI,E}}$. Then the position and velocity vectors in the Earth-centered inertial frame are transformed to $\boldsymbol{R}_{P,0}(t_{\text{out}}^{(1)})$, $\boldsymbol{V}_{P,0}(t_{\text{out}}^{(1)})$ in the Earth-centered ecliptic frame.

For the swingby, the position and velocity vectors of the spacecraft when it leaves or enters the kth planet's SOI, and the corresponding date, are determined by integrating the state of the spacecraft forward or backward from the periapsis at $t = t_{\text{GA},k}$. The orbital elements of the spacecraft at periapsis are calculated with $\boldsymbol{v}_\infty^\pm$ and periapsis radius r_p. Detailed expressions of the orbital elements can be found in the Appendix. With the orbital elements at the periapsis, $t_{\text{out}}^{(k+1)}$, $\boldsymbol{R}_{P,k}(t_{\text{out}}^{(k+1)})$ and $\boldsymbol{V}_{P,k}(t_{\text{out}}^{(k+1)})$ are obtained by integrating the EOM of an unpowered spacecraft forward until $||\boldsymbol{R}_{P,k}|| \geqslant r_{\text{SOI,P}}$. The quantities $t_{\text{in}}^{(k)}$, $\boldsymbol{R}_{P,k}(t_{\text{in}}^{(k)})$ and $\boldsymbol{V}_{P,k}(t_{\text{in}}^{(k)})$ are obtained by integrating the EOM of an unpowered spacecraft backward until $||\boldsymbol{R}_{P,k}|| \geqslant r_{\text{SOI,P}}$. The patched-arc model is illustrated in Figure 3. The general algorithm of the patched-arc model is presented in algorithm 1.

Algorithm 1. Algorithm of patched-arc model

Input: initial time t_0, final time t_f, launch $\boldsymbol{v}_{E\infty}$, swingby dates $t_{\text{GA},k}$, hyperbolic excess velocities $\boldsymbol{v}_{\infty,k}^\pm$ at swingbys, periapsis radius $r_{p,k}$ ($k = 1, 2, \ldots, n_0$)
Output: the fuel-optimal solutions of all low-thrust legs, the whole trajectory and the optimal thrust
Begin
  evaluate i_{park}, Ω_{park}, ω_{park} in an Earth-centered inertial frame and Δv_1, and transform orbital elements into state vector;
  calculate $t_{\text{out}}^{(1)}$, $\boldsymbol{R}_E^{\text{ECI}}(t_{\text{out}}^{(1)})$, $\boldsymbol{V}_E^{\text{ECI}}(t_{\text{out}}^{(1)})$ in Earth-centered inertial frame with a forward integration, and transform state vector into $\boldsymbol{R}_{P,0}(t_{\text{out}}^{(1)})$ $\boldsymbol{V}_{P,0}(t_{\text{out}}^{(1)})$ in planetocentric ecliptic reference frame;
  for $k = 1$ to n_0 **do**
    calculate the orbital elements at periapsis using $\boldsymbol{v}_{\infty,k}^\pm$ and periapsis radius $r_{p,k}$;
    obtain $t_{\text{out}}^{(k+1)}$, $\boldsymbol{R}_{P,k}(t_{\text{out}}^{(k+1)})$ $\boldsymbol{V}_{P,k}(t_{\text{out}}^{(k+1)})$, $t_{\text{in}}^{(k)}$, $\boldsymbol{R}_{P,k}(t_{\text{in}}^{(k)})$ and $\boldsymbol{V}_{P,k}(t_{\text{in}}^{(k)})$ with forward and backward integration;
  end
  for $k = 1$ to $n_0 + 1$ **do**
    set the boundary conditions with Equations (46) and (47);
    solve the fuel-optimal problem with the given boundary conditions;
  end
end

In this section, the design process has been introduced step by step. The design process is concluded as:

1. Selection of the number and sequence of swingbys based on Lambert problems. Compute the performances of impulsive transfer trajectories for all possible swingby sequences according to the process shown in Figure 2.
2. Search for feasible basic parameters of LTGA trajectories. Instead of directly solving the MPBVP in an indirect method, a global optimization algorithm is used to obtain solutions. Those solutions are not accurate enough for the MPBVP, but may be helpful to design an LTGA trajectory in this three-step approach. Then basic parameters are calculated with the solutions.
3. In order to design a trajectory with better performance, the search in step 2 is repeated many times. The performances of LTGA trajectories corresponding to all solutions in step 2 are briefly estimated with the patched-arc approach. However, in the estimation, to save computation time, only two-body dynamics is considered in low-thrust legs, while planetocentric legs are still governed by multi-body dynamics. Finally, the basic parameters with the best performance are used in the design of the LTGA trajectory in multi-body dynamics.

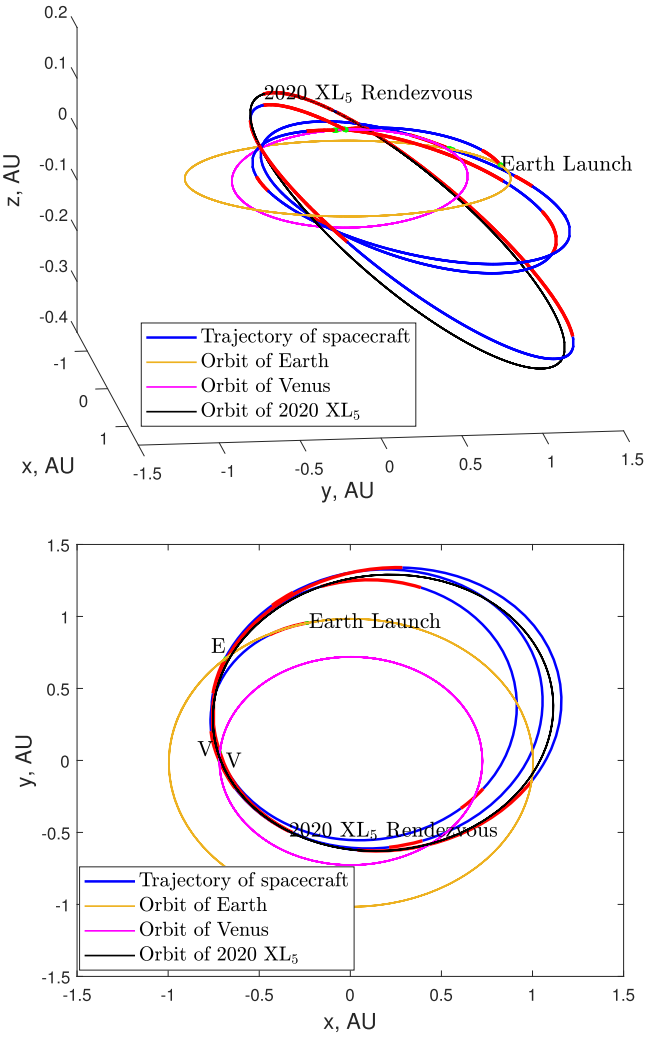

Figure 5. The LTGA trajectory in the heliocentric ecliptic reference frame corresponding to the Earth–Venus–Earth–Venus-2020 XL_5 swingby sequence. The orbits of Earth, Venus and the target asteroid 2020 XL_5 are displayed by lines with different colors; the red in the transfer trajectory means the legs where the thruster works, and the green in the transfer trajectory represents the planetocentric coasting legs.

3. Results

In this section, the rendezvous mission to 2020 XL_5 is designed through the three-step approach. First of all, the swingby sequence to 2020 XL_5 is determined. Second, the basic parameters for the LTGA trajectory are obtained through a global optimization. Finally, a more precise LTGA trajectory for a rendezvous mission to 2020 XL_5 is optimized in multi-body dynamics.

3.1. Swingby Sequence for Rendezvous to 2020 XL_5

The orbital elements of the ET 2020 XL_5 are listed in Table 1, which is provided by the MPC.[3]

[3] https://www.minorplanetcenter.net/data

Given that the synodic periods of Earth relative to Venus and Mars are respectively 1.6 yr and 2.1 yr (Takao et al. 2021), in the global search for swingby sequence, the departure epoch spans from 2024 January 1 to 2028 January 1, a range approximately twice the width of synodic periods to account for more possible sequences. All the flight times ΔT_0, ΔT_k vary between 10 and 1200 days. In previous work, it was emphasized that Venus and Earth are significant swingbys planets for rendezvous to asteroid 2010 TK_7 (Lei et al. 2017). Additionally, considering the large eccentricity of 2020 XL_5, with its distance from the Sun ranging from 0.6133 to 1.3881 au, Mars is also a favorable swingby planet. Therefore, Venus, Earth and Mars are designated as potential swingby planets. The minimum swingby altitudes for Venus, Earth and Mars are uniformly set as 200 km. The Keplerian elements of Venus, Earth/Moon barycenter and Mars are listed in Table 2. In this search, the Keplerian elements for Earth/Moon barycenter serve as an approximation of Earth's position. The maximum allowable total flight time for the rendezvous mission is set as $t_{f_{\max}} = 1200$ days. In the optimization of impulsive transfer trajectories for all the sequences using ICEA, the subpopulation allocated for the particle swarm optimization (PSO) algorithm is $NP_1 = 400$, while the subpopulation related to the differential evolution (DE) algorithm is $NP_2 = 100$. The number of generations is $N_G = 3000$. The penalty factors are set as $p_r = 10^5$ and $p_t = 10^3$. For this mission, the number of candidate swingby planets is $N_P = 3$, and the corresponding set is $\{P_0, P_1, P_2\} = \{\text{Venus, Earth, Mars}\}$. Given the mission's total flight time constraint of 1200 days, the maximum number of swingbys is restricted to $N_0 = 5$.

The computations are executed on a desktop personal computer with a CPU of 3.7 GHz, and Visual Studio 2019 is used. The best 10 results are listed in Table 3, where E denotes Earth, M means Mars and V signifies Venus. For those results, the constraints on swingby altitude and total flight time are satisfied. Moreover, for comparison, the direct transfer from Earth to asteroid 2020 XL_5 is optimized in the same way. The result is listed in Table 3 as well. Direct transfer to 2020 XL_5 requires a launch delta-v of 5.93 km s^{-1} and rendezvous delta-v of 4.40 km s^{-1}. Both of them are too large for the mission. According to this result, the multi-gravity assist technique greatly reduces the total delta-v for this mission. Mars is not an adequate swingby planet for the rendezvous mission to 2020 XL_5. Moreover, using Venus as the final swingby is the best option to reach asteroid 2020 XL_5. The swingby sequence Earth–Venus–Earth–Venus-2020 XL_5 is the best for this rendezvous mission, where the number of swingbys is $n_0 = 3$. Therefore, in the following parts, the LTGA trajectory corresponding to the Earth–Venus–Earth–Venus-2020 XL_5 sequence will be optimized. Before the optimization of the LTGA trajectory, the impulsive transfer trajectory corresponding to the Earth–Venus–Earth–Venus-2020 XL_5 sequence is further optimized with $N_G = 5000$, and related parameters are

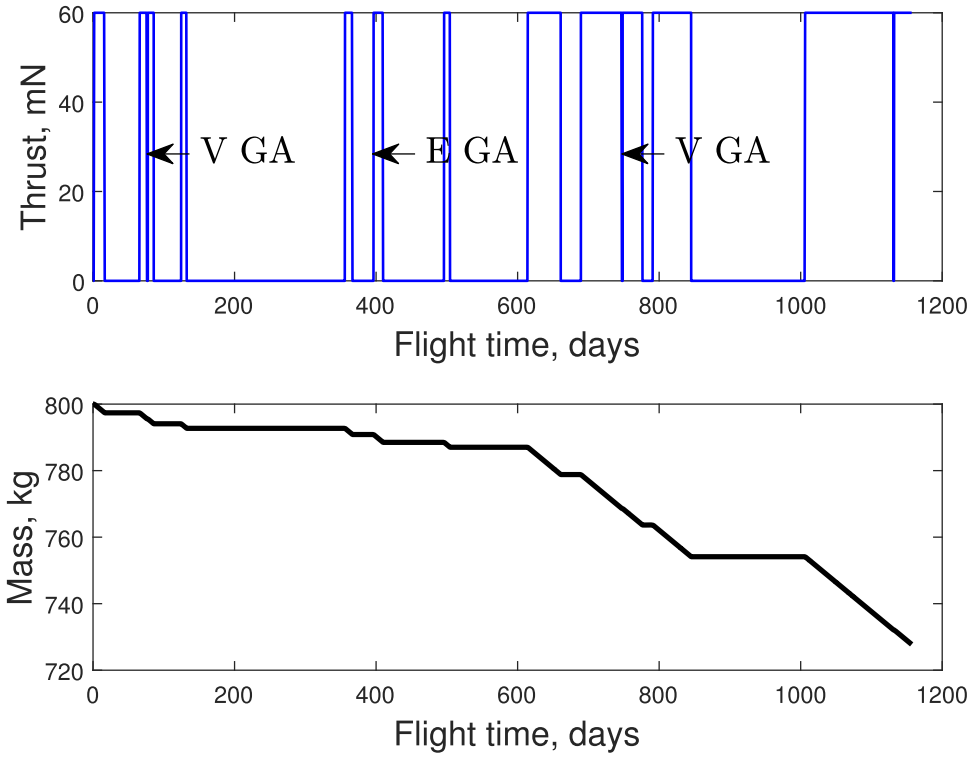

Figure 6. The time histories of the magnitude of thrust and spacecraft's mass corresponding to the Earth–Venus–Earth–Venus-2020 XL_5 swingby sequence.

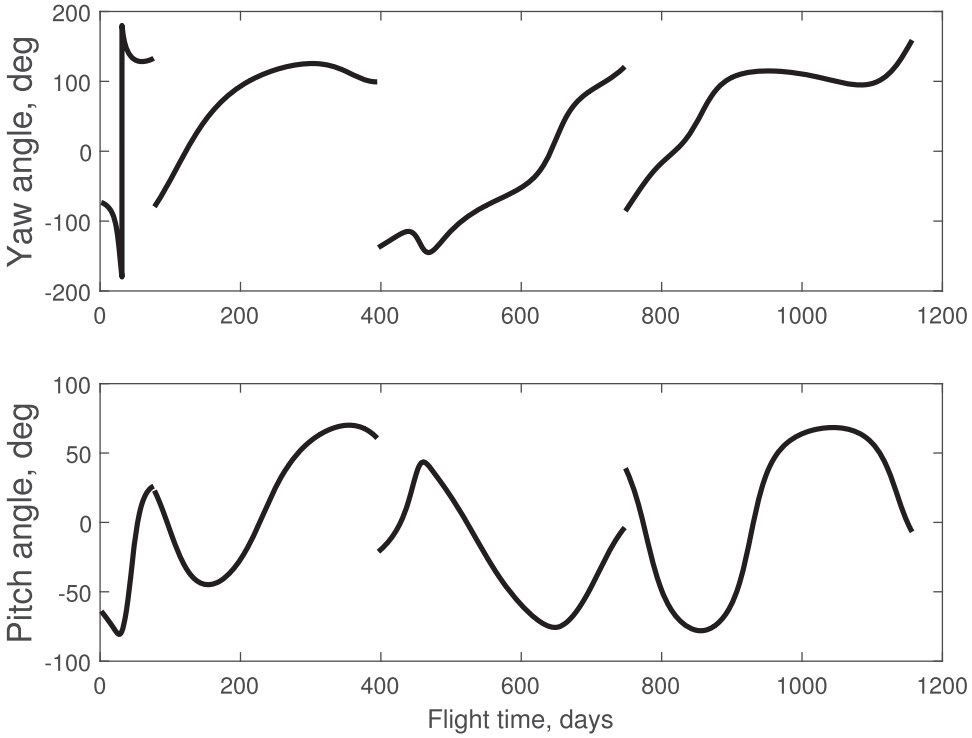

Figure 7. The time histories of the direction of thrust in the heliocentric ecliptic reference frame corresponding to the Earth–Venus–Earth–Venus-2020 XL_5 swingby sequence.

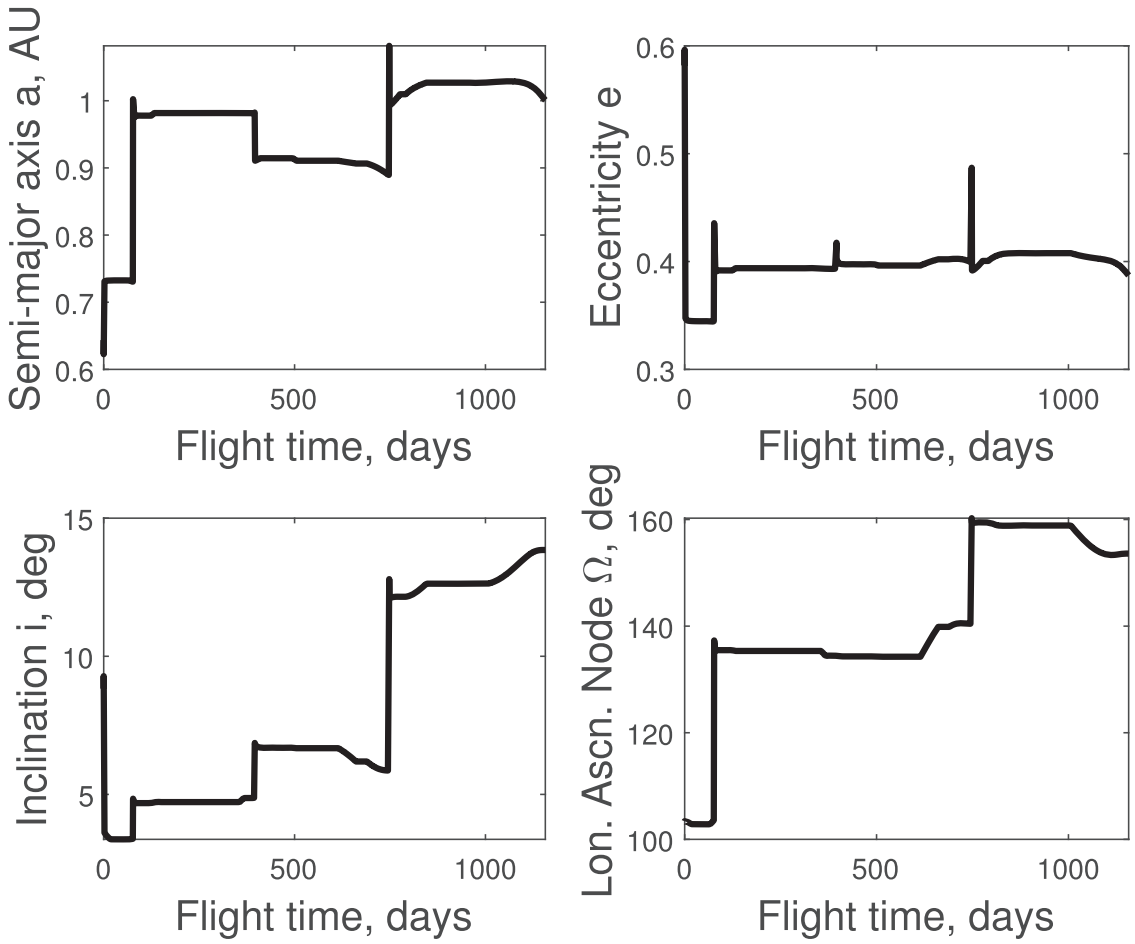

Figure 8. The time histories of orbital elements in heliocentric ecliptic reference frame including semimajor axis, eccentricity, inclination and longitude of ascending node corresponding to the Earth–Venus–Earth–Venus-2020 XL_5 swingby sequence.

Table 9
Parameters of Direct Low-thrust Transfer Trajectory from Earth to 2020 XL_5

Departure date (m/d/y)	2/15/2025
Departure delta-v, Δv_1 (km s^{-1})	5.00
Date leaving Earth's SOI (m/d/y)	2/16/2025
Norm of $\boldsymbol{V}_E(t_{\text{out}}^{(1)})$ (km s^{-1})	6.57
Rendezvous date (m/d/y)	10/9/2027
Flight time (days)	966.27
Propellant mass (kg)	166
Propellant mass ratio (%)	20.8

listed in Table 4. In Table 4, the propellant mass ratio is calculated by Mingotti et al. (2012)

$$\frac{m_p}{m_0} = 1 - \exp\left(-\frac{\Delta v_2 + \sum_{k=1}^{n_0}\Delta v_{\text{DSM}}^{(k)}}{I_{\text{spc}} g_0}\right), \tag{48}$$

where $I_{\text{spc}} = 300$ s is the specific impulse of the CP system, and m_p is the propellant mass. For the impulsive transfer trajectory corresponding to the Earth–Venus–Earth–Venus-2020 XL_5 sequence, the midcourse maneuvers at swingbys are relatively small. The propellant mass ratio is 44.51%. In order to save more propellant, low-thrust and multi-gravity assist techniques are applied in the following part. The optimal solutions of impulsive transfer trajectory are used to provide the upper and lower bounds of launch date, swingby dates and rendezvous date.

3.2. Global Search for Basic Parameters

In this mission, the maximal thrust magnitude of EP is $T_{\max} = 60$ mN, the specific impulse of EP is $I_{sp} = 3000$ s, the gravitational acceleration of Earth at sea level is $g_0 = 9.80665\,\text{m s}^{-2}$ and the initial mass of the spacecraft is $m_0 = 800$ kg. The states of planets are determined using the JPL ephemeris DE 421 (Folkner et al. 2009). The number of

Table 10
Position and Velocity Errors of the Low-thrust Trajectory for Different force Models

	Two-body Force	Gravitations of Sun, Venus, Earth, Mars and Jupiter
Position error of first leg	2.77×10^{-3}	4.88×10^{-5}
Velocity error of first leg	4.26×10^{-3}	9.69×10^{-5}
Position error of second leg	1.75×10^{-2}	1.83×10^{-5}
Velocity error of second leg	1.62×10^{-2}	1.00×10^{-5}
Position error of third leg	2.96×10^{-3}	1.59×10^{-5}
Velocity error of third leg	4.54×10^{-3}	3.23×10^{-5}
Position error of fourth leg	2.63×10^{-2}	1.61×10^{-5}
Velocity error of fourth leg	4.61×10^{-2}	2.72×10^{-5}

Note. Both position and velocity errors are nondimensionalized.

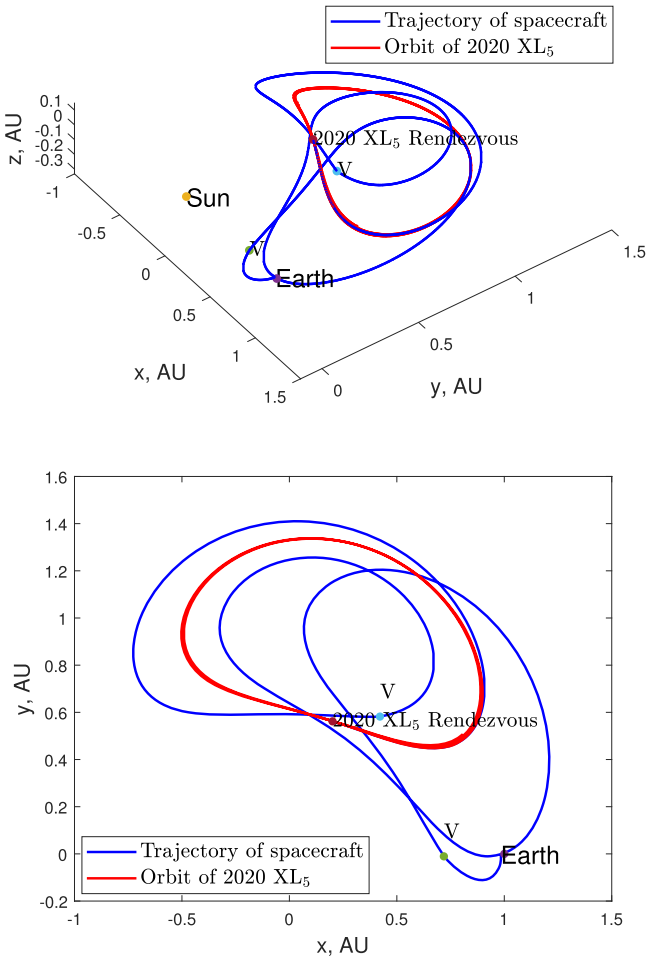

Figure 9. The LTGA trajectory in the synodic coordinate system corresponding to the Earth–Venus–Earth–Venus-2020 XL_5 swingby sequence.

generations $N_G = 100{,}000$, $NP_1 = 160$, $NP_2 = 40$. Referring to the optimized parameters of impulsive transfer trajectories, the launch date ranges from 1 October 2024 to 1 March 2025, flight time of spacecraft traveling from Earth to the first swingby planet ΔT_0 ranges from 50 to 100 days and flight times from the kth swingby planet to the next planet or asteroid ΔT_k all range from 300 to 500 days. Because the maximal gravity-assist impulse is the local circular speed at the minimal admissible periapsis radius (Sims 1996), which means $||\Delta \boldsymbol{v}_{G,k}||_{\max} = \sqrt{\mu_{P,k}/r_{p_{\min},k}}$, all magnitudes of the gravity-assist impulse range from 0 to 10 km s^{-1}. Considering the limit of the upper stage, the departure delta-v Δv_1 is assumed not to exceed the critical velocity $V_C = 5$ km s^{-1} for a payload of 800 kg (Lei et al. 2017). Thus, the launch $||\boldsymbol{v}_{E\infty}||$ is no more than 6.50 km s^{-1} according to Equation (1). The maximum total flight time is $t_{f_{\max}} = 1200$ days.

This search process is repeated for 40 times with these configurations. There are totally three solutions that can provide feasible basic parameters for optimization in the third step. The basic parameters are then derived with those solutions. The corresponding LTGA trajectories of these solutions are briefly estimated using the patched-arc approach, where only two-body dynamics is considered in low-thrust legs. In two-body dynamics, the minimum fuel consumption is 8.95% with a total flight time of 1157 days. The worst solution exhibits a fuel consumption of 10.4% with a total flight time of 1142 days. The convergence curves of these results are depicted in Figure 4. Theoretically, the convergence curve should converge to a value smaller than 1 where $f(\gamma) = m_p$ and $\Gamma = 0$. However, because of the critically small convergence domain of the multi-gravity assist problem, reaching this value through optimization is exceedingly challenging. According to the convergence curves, objective functions of these solutions all reach $20 \sim 30$. A large generation number is necessary for the objective function to reach a small value. It can have more of a chance to provide basic parameters that lead to converged transfer trajectories with better performances. Nevertheless, a larger number of generations is much more time-consuming. The basic parameters of the LTGA trajectory which has the minimum fuel consumption are listed in Table 5.

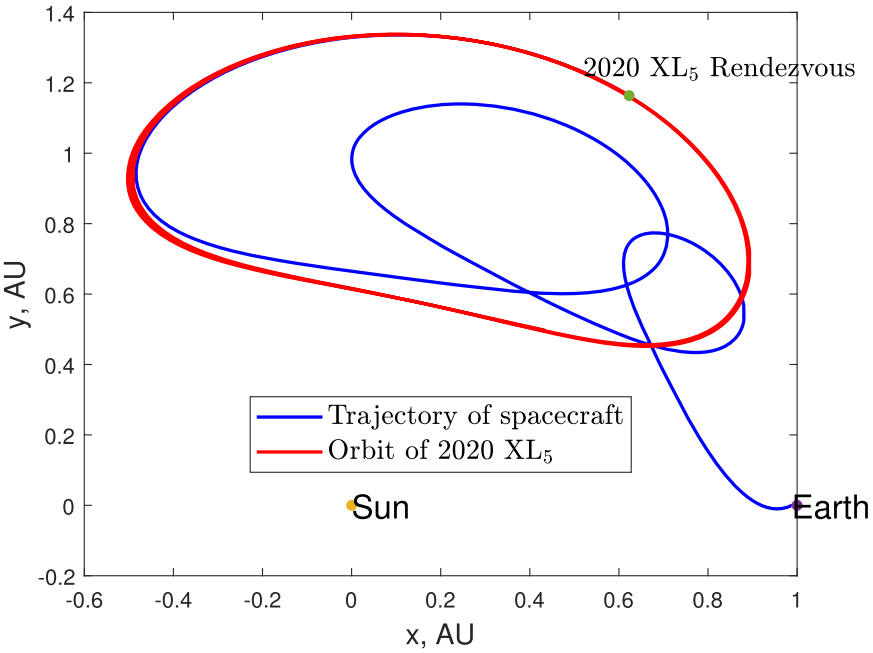

Figure 10. The direct low-thrust transfer trajectory in the synodic coordinate system corresponding to the Earth-2020 XL_5 sequence.

3.3. LTGA Trajectory from Earth to 2020 XL_5 in Multi-body Dynamics

In this mission, the semimajor axis of the parking orbit is $a_{\text{park}} = 6578.137$ km. The eccentricity is $e_{\text{park}} = 0$. The preferred inclination of the parking orbit is $i_0 = 28°.5$. The gravitations of the Sun, Venus, Earth, Mars and Jupiter are taken into account. With the basic parameters given in the last section, the LTGA trajectory is optimized in multi-body dynamics with algorithm 1. The orbital elements of the parking orbit and departure delta-v are listed in Table 6. The orbital elements of the hyperbolic trajectories at periapsis are listed in Table 7. Parameters of the LTGA trajectory are presented in Table 8. The trajectory of the spacecraft in the heliocentric ecliptic reference frame is depicted in Figure 5. Because the target asteroid 2020 XL_5 has a large inclination with respect to the ecliptic plane, the final Venus swingby must be performed around the date when Venus crosses the ascending or descending nodes of 2020 XL_5. This opportunity comes every 112.35 days, as the orbital period of Venus is about 224.7 days. This analysis is identical to the trajectory depicted in Figure 5. The time histories of the magnitude and direction of thrust and spacecraft's mass are shown in Figures 6 and 7. The time histories of orbital elements in the heliocentric ecliptic reference frame, including semimajor axis, eccentricity, inclination and longitude of ascending node, are displayed in Figure 8. As affirmed in Table 8, the total flight time is 1156.84 days, and the propellant mass ratio is 9.03%. The final mass of the spacecraft is 728 kg. For comparison, the direct transfer trajectory from Earth to 2020 XL_5 is optimized with the patched-arc model as well, whose parameters are presented in Table 9. As shown in Table 9, the total flight time is 966.27 days, which is 190.57 days shorter than the transfer with the multi-gravity assist technique. However, the propellant mass ratio is 20.8%. It means that the multi-gravity assist technique reduces the propellant mass ratio by 11.8%, corresponding to a saving of 94 kg in propellant mass. Therefore, the multi-gravity assist technique is significant for this mission to save the fuel consumption.

In order to show the influence of force models on the trajectory design result, the control laws derived from the two-body dynamics model and multi-body dynamics, including the gravitations of Sun, Venus, Earth, Mars and Jupiter, are respectively applied in the full gravitation system (gravitations of Sun, eight planets and the Moon). The position and velocity errors at the end of every leg are listed in Table 10. The position and velocity errors in Table 10 are both nondimensionalized. The results show that the control law derived from a two-body force model can lead to a large position and velocity errors ($\sim 10^{-2}$) at the end of every low-thrust leg, while the control law derived under multi-body dynamics, including gravitations of Sun, Venus, Earth, Mars and Jupiter, can keep the position and velocity errors around 10^{-5}. The inclusion of Mercury, planets outside Jupiter and the Moon will greatly increase the computation time for optimization of the transfer trajectory. Therefore, for the transfer trajectory to 2020 XL_5, a multi-body dynamics model, including gravitations of Sun,

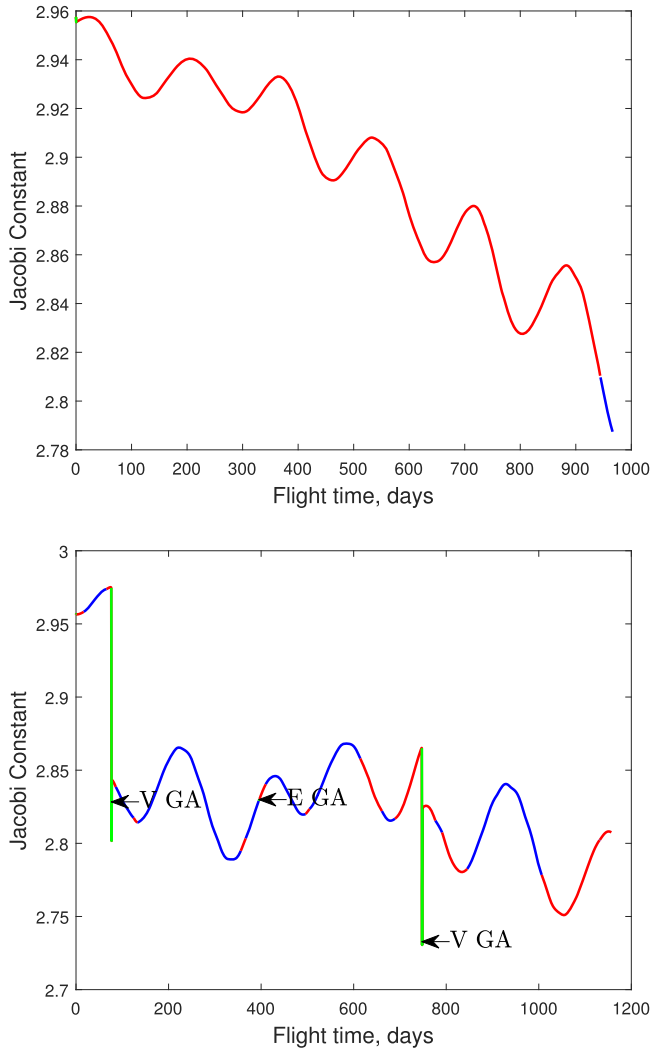

Figure 11. The Sun–Earth Jacobi constant of direct transfer trajectory (above) and LTGA trajectory (below). Red color means the parts where the thruster works, and green color in the transfer trajectory signifies the planetocentric coasting parts.

Venus, Earth, Mars and Jupiter, not only ensures accuracy, but also saves computation time.

For transfer to the ET asteroid, some characteristics in the Sun–Earth synodic coordinate system are significant. The trajectory of the spacecraft in the synodic coordinate system is depicted in Figure 9. The trajectory of direct transfer in the synodic coordinate system is shown in Figure 10 as well. In the Circular Restricted Three-Body Problem (CR3BP), the trajectories that lie along an unstable manifold of an L_1 orbit naturally approach the L_4 region (Elliott et al. 2020). In Figures 9 and 10, the two transfers both approach 2020 XL_5 through trajectories near the L_1 point. The Jacobi value represents a constant of motion within the rotating frame (Sood & Howell 2019). With the definition of Jacobi constant, a low value of the Jacobi constant is analogous to a higher energy for the spacecraft as it moves within the Sun–Earth system (Elliott et al. 2020). Although the Jacobi constant is only conserved in the CR3BP, and not in any higher-fidelity models, it is valuable in preliminary trajectory design activities. The spacecraft orbiting around Earth has a large value of Jacobi constant ($\sim$3). However, the target asteroid 2020 XL_5 is orbiting around the L_4 point with a low value of Jacobi constant ($\sim$2.8). From the viewpoint of energy, the transfer from Earth to 2020 XL_5 is challenging. The time histories of Jacobi constant of transfer with and without swingbys are both illustrated in Figure 11. For direct transfer, the thruster works for most of the flight to reach the desired Jacobi value. In contrast, employing multiple swingbys greatly reduces the Jacobi constant, requiring the thruster to work for a relatively shorter duration. It highlights the significance of the multi-gravity assist technique in reducing fuel consumption for this rendezvous mission. From the viewpoint of the Jacobi constant, Venus' first swingby reduces most of the Jacobi value (by $\sim$0.1), and Venus' second swingby reduces the Jacobi value by 0.04. Judging from the time histories of orbital elements in Figure 8, the semimajor axis, eccentricity and longitude of ascending node are mainly changed by Venus' first swingby, while the inclination is greatly changed by Venus' second swingby.

4. Conclusions

In this paper, a rendezvous mission to Earth's second ET asteroid 2020 XL_5 with low-thrust multi-gravity assist techniques is proposed. A three-step approach is introduced to design the LTGA trajectories in multi-body dynamics. The key conclusions of our study are as follows:

1. The direct impulsive transfer from Earth to 2020 XL_5 requires a total delta-v of 10.33 km s^{-1}, which is challenging for the capacity of current technology.
2. It is found that the best transfer sequence for a rendezvous mission to 2020 XL_5 is Earth–Venus–Earth–Venus-2020 XL_5. For the optimization of impulsive transfer trajectory corresponding to this sequence, the total delta-v is 6.26 km s^{-1}, with a fuel consumption of 44.51%. It highlights the potential of the multi-gravity assist technique in reducing both the launch energy and rendezvous delta-v for such a rendezvous mission. Moreover, Venus takes an important role in the rendezvous mission to 2020 XL_5.
3. The direct low-thrust transfer trajectory from Earth to 2020 XL_5 requires fuel consumption of 20.8%. This aspect emphasizes that the EP system is significant for saving fuel consumption in an interplanetary mission.
4. For the LTGA trajectory corresponding to the Earth–Venus–Earth–Venus-2020 XL_5 sequence, the fuel consumption is 9.03%, demonstrating the effectiveness of

combining EP and multi-gravity assist techniques compared to using either individually. Therefore, low-thrust multi-gravity assist techniques are recommended in the rendezvous mission to 2020 XL_5.

Acknowledgments

This work was supported by Basic Research Project of China (grant No: JCKY2020110C096) and the National Key R&D Program of China (grant No: 2020YFC2201202).

Appendix

In this appendix, some expressions about the conversion between launch $\boldsymbol{v}_\infty$ (transformed by $\boldsymbol{v}_{E\infty}$ from Earth-centered ecliptic reference frame to Earth-centered inertial frame) or swingby $\boldsymbol{v}_\infty^\pm$ and the orbital elements of the parking orbit or hyperbolic trajectory are listed.

For the parking orbit, the minimal admissible inclination is

$$i_{\min} = \arctan\left(\frac{|\boldsymbol{v}_{\infty,z}|}{\sqrt{\boldsymbol{v}_{\infty,x}^2 + \boldsymbol{v}_{\infty,y}^2}}\right),$$

where the subscripts x, y, z represent the three components of the vector in the reference frame. The longitude of ascending node Ω is given by

$$\Omega_{\text{park}} = \arctan\left(\frac{\boldsymbol{W}_{\text{park},x}}{-\boldsymbol{W}_{\text{park},y}}\right).$$

The quadrant of Ω_{park} is chosen according to the sign of $\boldsymbol{W}_{\text{park},x}$ and $-\boldsymbol{W}_{\text{park},y}$. Moreover, $\boldsymbol{W}$ is the unit vector of angular momentum, which is defined by

$$\boldsymbol{W} = \frac{\boldsymbol{r} \times \boldsymbol{v}}{||\boldsymbol{r} \times \boldsymbol{v}||}.$$

The x and y components of $\boldsymbol{W}_{\text{park}}$ are calculated by

$$\begin{cases} \boldsymbol{W}_{\text{park},z} = \cos i_{\text{park}}, \\ q_1 = \boldsymbol{v}_{\infty,x}^2 + \boldsymbol{v}_{\infty,y}^2, \\ q_2 = 2\boldsymbol{v}_{\infty,y}\boldsymbol{v}_{\infty,z}\boldsymbol{W}_{\text{park},z}, \\ q_3 = \boldsymbol{v}_{\infty,z}^2\boldsymbol{W}_{\text{park},z}^2 - \boldsymbol{v}_{\infty,x}^2 \sin^2 i_{\text{park}}, \end{cases}$$

$$\begin{cases} \boldsymbol{W}_{\text{park},y} = \frac{-q_2 \pm \sqrt{q_2^2 - 4q_1q_3}}{2q_1}, \\ \boldsymbol{W}_{\text{park},x} = -\frac{\boldsymbol{W}_{\text{park},y}\boldsymbol{v}_{\infty,y} + \boldsymbol{W}_{\text{park},z}\boldsymbol{v}_{\infty,z}}{\boldsymbol{v}_{\infty,x}}. \end{cases}$$

The two solutions of $\boldsymbol{W}_{\text{park},y}$ are both applicable. In this work, the solution $\boldsymbol{W}_{\text{park},y} = \frac{-q_2 - \sqrt{q_2^2 - 4q_1q_3}}{2q_1}$ is taken. The argument of perigee ω is obtained by

$$f_0 = \arccos\left(\frac{-\boldsymbol{v}_{\infty,x}\boldsymbol{W}_{\text{park},y} + \boldsymbol{v}_{\infty,y}\boldsymbol{W}_{\text{park},x}}{||\boldsymbol{v}_\infty|| \sin i_{\text{park}}}\right).$$

$$\begin{cases} \omega_{\text{park}} = f_0 - \arccos\left(-\frac{1}{1+||\boldsymbol{v}_\infty||^2 \frac{r_p}{\mu_E}}\right), & \text{if} \quad \boldsymbol{v}_{\infty,z} > 0 \\ \omega_{\text{park}} = 2\pi - f_0 - \arccos\left(-\frac{1}{1+||\boldsymbol{v}_\infty||^2 \frac{r_p}{\mu_E}}\right), & \text{if} \quad \boldsymbol{v}_{\infty,z} < 0 \end{cases}.$$

For the hyperbolic trajectory at swingby, the semimajor axis is

$$a_{\text{GA}} = \frac{\mu_P}{||\boldsymbol{v}_\infty^+||^2}.$$

Note that because the solution in Section 3 may not completely satisfy the constraints, there is a small error between $||\boldsymbol{v}_\infty^-||$ and $||\boldsymbol{v}_\infty^+||$, which is like the swingby with DSM illustrated in Figure 1. To obtain the hyperbolic trajectory without DSM, the orbital elements are evaluated mainly based on the last part of the hyperbolic trajectory where the spacecraft is going away from the planet, and $||\boldsymbol{v}_\infty^+||$ is used. The eccentricity, inclination and longitude of ascending node of the hyperbolic trajectory are expressed as

$$\begin{aligned} e_{\text{GA}} &= 1 + \frac{r_p}{a_{\text{GA}}}, \\ i_{\text{GA}} &= \arccos \boldsymbol{W}_{\text{GA},z}, \\ \Omega_{\text{GA}} &= \arctan\left(\frac{\boldsymbol{W}_{\text{GA},x}}{-\boldsymbol{W}_{\text{GA},y}}\right), \end{aligned}$$

where the unit vector of angular momentum $\boldsymbol{W}_{\text{GA}}$ is calculated by

$$\boldsymbol{W}_{\text{GA}} = \frac{\boldsymbol{v}_\infty^- \times \boldsymbol{v}_\infty^+}{||\boldsymbol{v}_\infty^- \times \boldsymbol{v}_\infty^+||}.$$

The quadrant of Ω_{GA} is chosen according to the sign of $\boldsymbol{W}_{\text{GA},x}$ and $-\boldsymbol{W}_{\text{GA},y}$. The argument of periapsis is

$$f_1 = \arccos\left(\frac{-\boldsymbol{v}_{\infty,x}^+\boldsymbol{W}_{\text{GA},y} + \boldsymbol{v}_{\infty,y}^+\boldsymbol{W}_{\text{GA},x}}{||\boldsymbol{v}_\infty^+|| \sin i_{\text{GA}}}\right).$$

$$\begin{cases} \omega_{\text{GA}} = f_1 - \arccos\left(-\frac{1}{e_{\text{GA}}}\right), & \text{if} \quad \boldsymbol{v}_{\infty,z}^+ > 0 \\ \omega_{\text{GA}} = 2\pi - f_1 - \arccos\left(-\frac{1}{e_{\text{GA}}}\right), & \text{if} \quad \boldsymbol{v}_{\infty,z}^+ < 0 \end{cases}.$$

The true anomaly is zero at the periapsis.

References

Bate, R. R., Mueller, D. D., White, J. E., & Saylor, W. W. 2020, Fundamentals of Astrodynamics (Mineola, NY: Courier Dover Publications)
Bertrand, R., & Epenoy, R. 2002, OCAM, 23, 171
Casalino, L., Colasurdo, G., & Pastrone, D. 1999, JGCD, 22, 637
Chen, S., Li, H., & Baoyin, H. 2018, Ap&SS, 363, 128
Connors, M., Wiegert, P., & Veillet, C. 2011, Natur, 475, 481

de La Fuente Marcos, C., & de La Fuente Marcos, R. 2013, MNRAS: Letters, 432, L31
De la Fuente Marcos, C., & de la Fuente Marcos, R. 2014, MNRAS, 439, 2970
de la Fuente Marcos, C., & de la Fuente Marcos, R. 2015, MNRAS, 453, 1288
de la Fuente Marcos, C., & de la Fuente Marcos, R. 2021, RNAAS, 5, 29
Dvorak, R., & Schwarz, R. 2005, CeMDA, 92, 19
Elliott, I., Sullivan, C., Jr, Bosanac, N., Stuart, J. R., & Alibay, F. 2020, JGCD, 43, 1854
Englander, J. A., & Conway, B. A. 2017, JGCD, 40, 15
Fehlberg, E. 1968, NASA Technical Report , R-287
Folkner, W. M., Williams, J. G., & Boggs, D. H. 2009, IPN Progress Report, 42, 1
Gao, Y., & Kluever, C. 2004, Collection of Technical Papers—AIAA/AAS Astrodynamics Specialist Conference, 2, 5088
Gao, Y., Lu, X., Peng, Y., Xu, B., & Zhao, T. 2019, AdSpR, 63, 432
Gobetz, F. W. 1963, AIAAJ, 1, 2034
Gooding, R. 1990, CeMDA, 48, 145
Haberkorn, T., Martinon, P., & Gergaud, J. 2004, JGCD, 27, 1046
Hargraves, C. R., & Paris, S. W. 1987, JGCD, 10, 338
Hui, M.-T., Wiegert, P. A., Tholen, D. J., & Föhring, D. 2021, ApJL, 922, L25
Hull, D. G. 2013, in Optimal Control Theory for Applications, ed. F. Ling Frederick (New York, NY: Springer)
Jiang, F., Baoyin, H., & Li, J. 2012, JGCD, 35, 245
Johnson, F. T. 1969, AIAAJ, 7, 993
Lei, H., Xu, B., & Sun, Y. 2013, AdSpR, 51, 917
Lei, H., Xu, B., & Zhang, L. 2017, AdSpR, 60, 2505
Lifset, N., Golovich, N., Green, E., Armstrong, R., & Yeager, T. 2021, AJ, 161, 282
Malhotra, R. 2019, NatAs, 3, 193
Markwardt, L., Gerdes, D. W., Malhotra, R., et al. 2020, MNRAS, 492, 6105
Martinon, P., & Gergaud, J. 2010, PhD thesis, INRIA
McConaghy, T. T., Debban, T. J., Petropoulos, A. E., & Longuski, J. M. 2003, JSpRo, 40, 380
Melbourne, W., & Sauer, C., Jr 1965, in Supporting Research and Advanced Development, Space Programs Summary 37, 36, 14, 36 (Pasadena, CA: California Institute of Technology) 14–19
Mingotti, G., Topputo, F., & Bernelli-Zazzera, F. 2012, CNSNS, 17, 817
Morante, D., Sanjurjo Rivo, M., & Soler, M. 2021, Aeros, 8, 88
Nicholson, S. B. 1961, ASPL, 8, 239
Okutsu, M., Yam, C. H., & Longuski, J. 2006, in Low-Thrust Trajectories to Jupiter via Gravity Assists from Venus, Earth, and Mars (Keystone, CO: AIAA/AAS Astrodynamics Specialist Conference and Exhibit), 6745
Olympio, J. 2008, PhD thesis, Citeseer
Petropoulos, A. E., & Longuski, J. M. 2004, JSpRo, 41, 787
Petropoulos, A. E., Longuski, J. M., & Vinh, N. X. 2000, AsDyn, 1999, 563
Pierson, B. L., & Kluever, C. A. 1994, JGCD, 17, 1275
Powell, M. J. 1970, A hybrid method for nonlinear equations, in Numerical Methods for Nonlinear Algebraic Equations, ed. P. Rabinowitz (London: Gordon & Breach Science Pub) 87–114
Santana-Ros, T., Micheli, M., Faggioli, L., et al. 2022, NatCo, 13, 447
Sheppard, S. S., & Trujillo, C. A. 2006, Sci, 313, 511
Sims, J. A. 1996, PhD thesis, Purdue Univ.
Sood, R., & Howell, K. 2019, JAnSc, 66, 247
Takao, Y., Mori, O., Matsushita, M., & Sugihara, A. K. 2021, AcAau, 181, 362
Vasile, M., & Campagnola, S. 2009, JBIS, 62, 15
Whiteley, R. J., & Tholen, D. J. 1998, Icar, 136, 154
Wiegert, P., Innanen, K., & Mikkola, S. 2000, Icar, 145, 33
Wiegert, P. A., Innanen, K. A., & Mikkola, S. 1997, Natur, 387, 685
Xu, R., Cui, P., Qiao, D., & Luan, E. 2007, AdSpR, 40, 220
Yang, H., Li, J., & Baoyin, H. 2015, AdSpR, 56, 837
Zhang, C., Topputo, F., Bernelli-Zazzera, F., & Zhao, Y.-S. 2015, JGCD, 38, 1501